

POLITECNICO DI MILANO

Scuola di Ingegneria Industriale e dell'Informazione



1-D FLUID DYNAMIC SIMULATION OF IC ENGINES WITH SHORT AND LONG EGR CIRCUITS

Tesi di laurea di:

Gianmarco Belotti Matr. 884382

Relatore: Prof. Onorati Angelo

Anno accademico 2017/2018

Ringraziamenti

Desidero ringraziare innanzitutto il prof. Onorati, che ha avuto la pazienza e la capacità di guidarmi in questo lavoro, anche quando io per primo iniziavo a crederci ben poco. I miei familiari, che mi hanno permesso di raggiungere questo traguardo, sostenendomi sempre e ricordandomi che si può sempre migliorare.

Martina, che ha avuto la pazienza di non prendermi a male parole nonostante la tesi ci tenesse distanti.

I soci sia in valle che qua nella nebbia, grazie per la fonte inesauribile di ristoro mentale ed eventuali serate alcoliche.

A special thanks to Dylan, who helped me in the first part of this work and introduced me in the magical GasDyn world, I hope some day we will meet again!

ABSTRACT

In this thesis work it has been studied the possibility of implementing an Exhaust Gas Recirculation (EGR) circuit on a modern, downsized, turbocharged spark ignition engine.

The results are found using one-dimensional gas-dynamic numerical modelisation, thanks to the GasDyn program, a computational code developed in Politecnico di Milano that can simulate the functioning of an internal combustion engine in its whole components, so even all the ducts, valves and heat exchangers that are necessary to the engine's work.

The main goal of the work is to demonstrate that the application of the EGR on a spark ignition engine, facing the actual and future pollution normatives, is possible and can help reducing the noxious emissions, wich are more and more strictly as the years passes.

INTRODUZIONE

In questo lavoro di tesi è stata studiata la possibilità di implementare un circuito di ricircolo gas di scarico (EGR) su un motore ad accensione comandata di tipo turbocompresso.

I risultati sono stati ricavati mediante simulazione fluidodinamica monodimensionale utilizzando il programma GasDyn, sviluppato dal Politecnico di Milano, il quale è in grado di simulare il funzionamento di un motore a combustione interna nella sua completezza, cioè comprendendo tutte le componenti ausiliarie quali condotti, valvole e scambiatori di calore.

L'obiettivo principale è dimostrare che l'applicazione di un EGR su un motore a benzina, considerando le normative antiinquinamento attuali e future, è possibile e può effettivamente aiutare a ridurre le emissioni nocive, i cui limiti diventano più stringenti di anno in anno.

Summary

1-D FLUID DYNAMIC SIMULATION OF IC ENGINES WITH SHORT AND LONG EGR CIRCUITS	I
RINGRAZIAMENTI	I
ABSTRACT	III
INTRODUZIONE	IV
SUMMARY	V
LIST OF FIGURES	VII
LIST OF TABLES.....	X
CHAPTER 1 GOVERNING EQUATIONS AND COMPUTATIONAL METHODS.....	11
1.1 GOVERNING EQUATIONS	11
1.1.1 <i>Mass conservation equation</i>	12
1.1.2 <i>Momentum conservation equation</i>	13
1.1.3 <i>Energy conservation equation</i>	14
1.1.4 <i>Closure equations</i>	15
1.1.5 <i>Equations in conservative form</i>	16
1.2 COMPUTATIONAL METHODS	17
1.2.1 <i>Method of characteristics</i>	18
1.2.2 <i>Shock capturing methods</i>	30
1.2.3 <i>Lax-Wendroff method</i>	31

1.2.4 MacCormack method.....	34
1.2.5 Spurious oscillations problem.....	35
CHAPTER 2: INTRODUCTION AND FUNCTIONING OF GASDYN	
.....	41
2.1 INTRODUCTION TO GASDYN.....	41
2.1.1: Instantaneous heat fluxes	42
2.1.2 In-cylinder turbulence.....	43
2.2 SPARK IGNITION ENGINES.....	45
2.2.1 Cylinder charge model	45
2.2.2 Predicting combustion models	46
2.3 PREDICTING EMISSIONS MODEL.....	49
2.3.1 Carbon monoxide (CO).....	49
2.3.2 Nitric oxides (NO).....	50
2.3.3 Unburned hydrocarbon (HC).....	51
CHAPTER 3: TURBOCHARGED ENGINE AND GASDYN	
MODELING	54
3.1 THE TURBOCHARGED ENGINE	54
3.1.1: Turbocharger implementation in Gasdyn.....	56
CHAPTER 4: EMISSIONS AND EGR SYSTEM.....	60
4.1: POLLUTANT EMISSIONS.....	60
4.2: EGR SYSTEM.....	63
CHAPTER 5: ENGINE VALIDATION AND SIMULATIONS	65
5.1: ENGINE VALIDATION.	65
5.2: PART LOAD AND EGR MODELS IMPLEMENTATION.....	68
5.2.1: Part load model.....	68
5.2.2: Short route EGR system.....	71
5.2.3: Long Route EGR system.....	77
BIBLIOGRAPHY.....	85

List of figures

Figure 1. 1: One-dimensional approach for the computational process.	12
Figure 1. 2: Graphical representation of method of characteristics.	18
Figure 1. 3: characteristic lines drawn into the discretized (x,t) space	20
Figure 1. 4: Position and state diagrams for the Riemann variables.	22
Figure 1. 5: a/s diagram for recognizing the value of a_{ref} .	23
Figure 1. 6: the effects on a point P due to the previous conditions in C,D,F	26
Figure 1. 7: example of computational process in a space/time grid	28
Figure 1. 8: design of the characteristic lines. The path line is the central one, that intersecates the time Z axis in the point s.	28
Figure 1. 9: two-step Lax-Wendroff method computational scheme	33
Figure 1. 10: MacCormack forward predictor-backward corrector computational scheme	35
Figure 2.1: GasDyn schematics of a 4 cylinder N/A engine	41
Figure 2.2: zero-dimensional energy cascade	43
Figure 2. 3: multi-zone approach for spark ignition engines.	45
Figure 2. 4: Cylinder pressure and burned mass fraction represented using a Wiebe curve	47
Figure 2. 5: crevice volume	51
Figure 3. 1: Turbocharged 4-cylinder engine, with intercooler and waste-gate valve. Notice that the turbine and the compressor have a common shaft, wich has to bring the mechanical power from the turbine to the compressor.	55
Figure 3. 2: Example of interpolated curves for a compressor.	56
Figure 3. 3: Turbine curves afert data extrapolation.	58
Figure 4. 1: Composition of the NEDC homologation test.	61
Figure 4. 2: WLTC cycle for Class 2 vehicles, with a PMR between 22 and 34.	62

Figure 4. 3: Euro emission limits for spark ignition engines.	62
Figure 4. 4: effect of the air/fuel ratio on the NOx production.	63
Figure 4. 5: Example of an EGR (exhaust gas recirculation) system.	63
Figure 5. 1: Alfa Romeo 1.8 TBi engine	65
Figure 5. 2: Engine model into the GasDyn editor.	66
Figure 5. 3: Comparison between experimental and computer performances of the engine: the higher ones are the torque curves, and the lower ones the power curves.	67
Figure 5. 4: Convergence of the compressore and turbine power.	67
Figure 5. 5: Torque at part load compared with the full load curve	69
Figure 5. 6: Engine power at part load compared with the full load curve.	69
Figure 5. 7: Boost pressure at full load and part load.	70
Figure 5. 8: Throttle opening at full load and part load	70
Figure 5. 9: NOx emissions without EGR.	71
Figure 5. 10: GasDyn editor view of the short route EGR.	71
Figure 5. 11: Torque comparison between the three cases.	72
Figure 5. 12: throttle opening angles for the three different layout.	73
Figure 5. 13: target boost pressure for the three different layout.	73
Figure 5. 14: Average NOx emissions on the four cylinders at different EGR rates.	74
Figure 5. 15: in-cylinder temperatures at 1500 rpm at different recirculation rates	75
Figure 5. 16: in-cylinder temperatures at 2000 rpm at different recirculation rates.	76
Figure 5. 17: in-cylinder temperatures at 4500 rpm at different recirculation rates.	76
Figure 5. 18: Long route scheme on GasDyn editor.	77
Figure 5. 19: Boost target pressure for the three main cases.	78
Figure 5. 20: Throttle opening for the three main cases.	78

Figure 5. 21: Torque comparison between standard and long route working points.	79
Figure 5. 22: Compressor working points in the m'_{rid} /compressor ratio plain.	80
Figure 5. 23: Inlet gases temperature at 2000 rpm.	81
Figure 5. 24: Inlet gases temperature at 4500 rpm.	81
Figure 5. 25: NOx emission comparison between long route and short route.	82
Figure 5. 26: In-cylinder temperature at 2000 rpm.	83
Figure 5. 27: In-cylinder temperature at 3500 rpm.	83
Figure 5. 28: In-cylinder temperature at 4500 rpm.	83

List of tables

Table 5. 1: Characteristics of the 1.8 TBi engine.	66
Table 5. 2: Mass of fuel injected and spark advance for the investigated regimes	70
Table 5. 3: Difference between real and target recirculation rate.	74
Table 5. 4: Real recirculation ratios for short and long route.	78

CHAPTER 1

GOVERNING EQUATIONS AND COMPUTATIONAL METHODS

1.1 Governing equations

An internal combustion engine is a cyclic, thermal machine composed by the “proper” engine, made by the cylinders, and the inlet and exhaust ducts that have to bring in and out from the engine the working fluids.

Due to the cyclic behaviour, all the flows that characterize the engine working points are highly unsteady, and so the computation of the fluid properties, which are fundamental for evaluating the engine performances requires the solution of very complex differential equations, possible using numerical methods.

These methods need a huge computational power that nowadays is not affordable, so the process is made under the following hypothesis that can lower the computational effort:

- Unsteady flows,
- Compressible flows,
- One-dimensional flows,
- Low sections variations along the ducts,
- Non-adiabatic process,

- Non-homentropic process,
- Thermal and friction effects considered only at the boundaries.

The approach on the definition of the main equations is still differential, but the only dimation considered is now the axial coordinate of the ducts, using an eulerian representation of the flow as showed in figure 1.

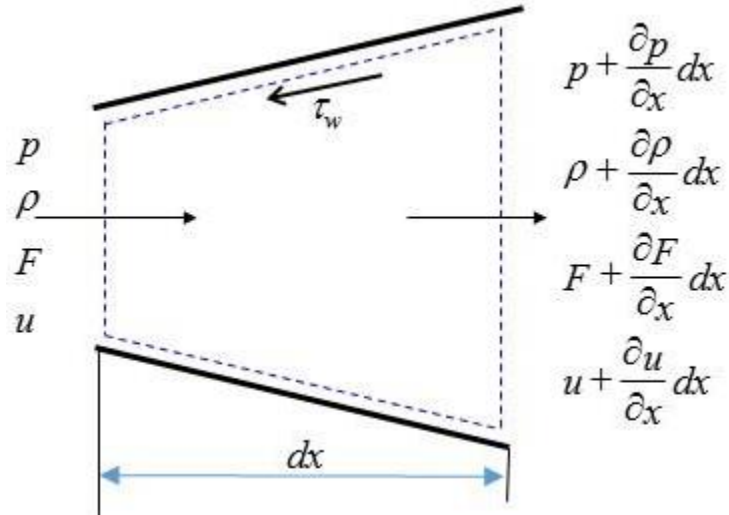


Figure 1. 1: One-dimensional approach for the computational process.

We have three fundamental governing equations:

1.1.1 Mass conservation equation

This equation gives the rate of mass change into the control volume, wich is equal to the net mass flow through the element:

$$\frac{\partial(\rho F dx)}{\partial t} = \frac{\partial(\rho u F)}{\partial x} dx \quad (1.1)$$

Where dx is the infinitesima length of a duct, F the cross-sectional area.

The derivatives can be expanded, obtaining the following equation:

$$\left(\rho + \frac{\partial \rho}{\partial x} dx\right) \left(u + \frac{\partial u}{\partial x} dx\right) \left(F \frac{\partial F}{\partial x} dx\right) - \rho u F = - \frac{\partial(\rho F dx)}{\partial t} \quad (1.2)$$

Rearranging the terms and considering only the first-order derivatives, the equation is simplified as:

$$\frac{\partial \rho}{\partial t} + \rho \frac{\partial u}{\partial x} + u \frac{\partial \rho}{\partial x} + \frac{\rho u}{F} \frac{dF}{dx} = 0 \quad (1.3)$$

1.1.2 Momentum conservation equation

This equation keeps in account the fact that the sum of the pressure and shear stress on the boundary of control volume is equal to the rate of increase of momentum of the fluid particle, so we have:

- Pressure contribution, due to the difference of pressure on the end faces and the component on the axial direction of the pressure acting on the sides of the control volume:

$$pF - \left(p + \frac{\partial p}{\partial x} dx \right) \left(F + \frac{\partial F}{\partial x} dx \right) + p \frac{\partial F}{\partial x} dx = - \frac{\partial(pF)}{\partial x} dx + p \frac{\partial F}{\partial x} dx \quad (1.4)$$

- The shear stress given by the friction between the moving fluid and the stationary walls that represent the boundaries of the ducts, which is computed as a “ τ_w ” stress acting in a direction opposite to the flow:

$$\tau_w = \frac{1}{2} \rho f u^2 \quad (1.5)$$

This has to be applied on the entire cross-sectional area, so we find a “friction force” computed as following:

$$F_{friction} = - \frac{1}{2} \rho f u^2 (\pi D dx) \quad (1.6)$$

- The rate of momentum increase, which is computed as:

$$\frac{\partial(\rho u F dx)}{\partial t} dx \quad (1.7)$$

- The net efflux of momentum on the control area:

$$\frac{\partial(\rho F u^2 dx)}{\partial x} \quad (1.8)$$

Keeping in account all these components, the momentum conservation equation can be written as:

$$-\frac{\partial(pF)}{\partial x} dx + p \frac{dF}{dx} dx - \frac{1}{2} \rho u^2 f \pi D dx = \frac{\partial(u\rho F dx)}{\partial t} + \frac{\partial(\rho F u^2)}{\partial x} dx \quad (1.10)$$

Then, expanding the derivatives, considering the continuity and re-arranging the equation the following form is found:

$$\frac{\partial u}{\partial t} + u \frac{\partial u}{\partial x} + \frac{1}{\rho} \frac{\partial \rho}{\partial x} + G = 0 \quad (1.11)$$

Where:

$$G = f \frac{u^2}{2} \frac{u}{|u|} \frac{4}{D} \quad (1.12)$$

1.1.3 Energy conservation equation

This equation is derived from the application of the first law of thermodynamics to the control volume, in the form:

$$Q \cdot - W_s \cdot = \frac{\partial E_0}{\partial t} + \frac{\partial H_0}{\partial x} dx \quad (1.13)$$

The equation can be written using the specific quantities referred to mass, obtaining:

$$\frac{\partial(e_0 \rho F dx)}{\partial t} + \frac{\partial(h_0 \rho F u)}{\partial x} dx = \frac{\partial q}{\partial t} \rho F dx + \Delta H_{react} F dx \quad (1.14)$$

Where:

- $e_0 = e + \frac{1}{2} u^2$, the total specific internal energy;
- $h_0 = e + \frac{p}{\rho}$, the total specific enthalpy;
- q is the heat transfer rate per mass unit;
- ΔH_{react} is the reaction enthalpy related to the possible chemical reactions happening in the ducts.

1.1.4 Closure equations

Since the system is composed by three equations but faces four variables (p , ρ , u , e) there's the need of another equation that can allow to solve it, which is represented by the equation of state of the gas flowing in the pipes.

Due to the gas properties, the perfect gas equation can be suitable:

$$\frac{p}{\rho} = RT \quad (1.15)$$

This equation introduces another variable, the temperature T , but brings back even the benefit that for a perfect gas we can assume that both internal energy and enthalpy are temperature-related, in order to write:

$$e = e(T) = C_v T \quad (1.16)$$

And

$$h = h(T) = e + RT = C_p T \quad (1.17)$$

where C_p , C_v are the specific heat capacities, that have the property valid for perfect gas to be written as a ratio which gives a constant:

$$\frac{C_p}{C_v} = k \quad (1.18)$$

The two specific capacities are also related to the specific gas constant, so it's possible to write:

$$C_v = \frac{R}{k - 1} \quad (1.19)$$

$$C_p = \frac{kR}{k - 1} \quad (1.20)$$

This allows finally to write energy and enthalpy as a function of the previous variables and close the system, because the energy equation can be written now as:

$$\begin{aligned} \frac{\partial}{\partial t} \left[(\rho F dx) \left(C_v T + \frac{u^2}{2} \right) \right] + \frac{\partial}{\partial x} \left[(\rho F dx) \left(C_v T + \frac{p}{\rho} + \frac{u^2}{2} \right) \right] dx \\ = \frac{\partial q}{\partial t} \rho F dx + \Delta H_{react} F dx \end{aligned} \quad (1.21)$$

Which, combined with the continuity and the momentum equation, gives the following form, where all the products have been solved:

$$\left(\frac{\partial p}{\partial t} + u \frac{\partial p}{\partial x}\right) - a^2 \left(\frac{\partial p}{\partial t} + u \frac{\partial p}{\partial x}\right) - \rho(k-1) \left(\frac{\partial q}{\partial t} - \frac{\Delta H_{react}}{\rho} + uG\right) = 0 \quad (1.22)$$

Written in non-conservative form, where:

- a is the speed of sound, function of the gas temperature in homentropic conditions;

After all the system made of hyperbolic equations written in non-conservative form is the following:

$$\frac{\partial \rho}{\partial t} + \frac{\partial}{\partial x}(\rho u) + \frac{\rho u}{F} \frac{dF}{dx} = 0 \quad (1.3)$$

$$\frac{\partial u}{\partial t} + u \frac{\partial u}{\partial x} + \frac{1}{\rho} \frac{\partial p}{\partial x} + G = 0 \quad (1.10)$$

$$\left(\frac{\partial p}{\partial t} + u \frac{\partial p}{\partial x}\right) - a^2 \left(\frac{\partial p}{\partial t} + u \frac{\partial p}{\partial x}\right) - \rho(k-1) \left(\frac{\partial q}{\partial t} - \frac{\Delta H_{react}}{\rho} + uG\right) = 0 \quad (1.22)$$

$$\frac{p}{\rho} = RT \quad (1.15)$$

$$e = C_v T \quad (1.16)$$

1.1.5 Equations in conservative form

In order to obtain a high level of accuracy of the solutions, the computational process passes through the use of shock-capturing methods, that needs to adopt the equations in their conservative form.

This means that is necessary to identify the variables that remains constant, due to the fact that they're used for solving the problem around the discontinuities that can emerge in the flow.

So, the system has to be re-written in function of these constant variables, obtaining the following equations set ("strong conservative form").

$$\frac{\partial(\rho F)}{\partial t} + \frac{\partial(\rho u F)}{\partial x} = 0 \quad (1.23)$$

$$\frac{\partial(\rho u F)}{\partial t} + \frac{\partial(\rho u^2 F + p F)}{\partial x} - p \frac{\partial F}{\partial x} + \rho G F = 0 \quad (1.24)$$

$$\frac{\partial(\rho e_0 F)}{\partial t} + \frac{\partial(\rho u h_0 F)}{\partial x} - \rho \frac{\partial q}{\partial t} F - \Delta H_{react} F = 0 \quad (1.25)$$

An important advantage of this form is that it can be written even in matrix form, and so the system can be compacted into an only equation as follows:

$$\frac{\partial \bar{w}(x, t)}{\partial t} + \frac{\partial \bar{F}(\bar{w})}{\partial x} + \bar{B}(\bar{w}) + \bar{C}(\bar{w}) = 0 \quad (1.26)$$

Where it can be found the following vectors:

- Conservative variables vector:

$$\bar{w} = \begin{vmatrix} \rho F \\ \rho u F \\ \rho e_0 F \end{vmatrix} \quad (1.27)$$

- Fluxes vector:

$$\bar{F} = \begin{vmatrix} \rho u F \\ (\rho u^2 + p) F \\ \rho u h_0 F \end{vmatrix} \quad (1.28)$$

- Source term vector due to the pipe cross-section change:

$$\bar{B}(\bar{W}) = \begin{vmatrix} 0 \\ -p \frac{dF}{dx} \\ 0 \end{vmatrix} \quad (1.29)$$

- Source term vector due to fluid friction and heat transfer into the control volume:

$$\bar{c}(\bar{W}) = \begin{vmatrix} 0 \\ \rho G F \\ -(q\rho + \Delta H_{react}) F \end{vmatrix} \quad (1.30)$$

1.2 Computational methods

The main problem related to the governing equations system is that is non possible to determine a solution for that kind of hyperbolic system by an analytical way.

The solution of these problem passes so through a numerical approximation, and the first studies about that were made by Riemann in 1858, with the developing of the “method of characteristics”, that has been widely used until the ‘80s of the last century, when more accurate “shock-capturing” methods were implemented.

1.2.1 Method of characteristics

Therefore actually the most important solving methods are the shock-capturing ones, this method is still used for the modeling of the border conditions of the pipes, despite some limitations due mainly to the following three facts:

- The gas is modeled as a perfect gas with constant specific heat;
- It is a first-order of accuracy method, and the space-time domain is represented into a linearly approximated grid;
- It is not able to recognise discontinuities (shock-waves) into the solution.

This method is characterized by the fact that can transform partial derivatives into total derivatives, by moving along some particular lines through the flux, called “characteristic lines”.

As an example, it could be considered an equation in the form:

$$c = c(x, t) \tag{1.31}$$

That gives a surface into the (x,t,c) space, considering as a reference c=0.

Now, considering a line that connects two points A and B on this surface and its projection on the plan c=0, it can be called “characteristic line” if in every point the slope (angular coefficient) of the projection has the same numerical value of the function in the same point, so that:

$$\left(\frac{dx}{dt}\right)_{m'} = c(x, t)_{m'} = \overline{mm'} \tag{1.32}$$

As shown in figure 1.2.

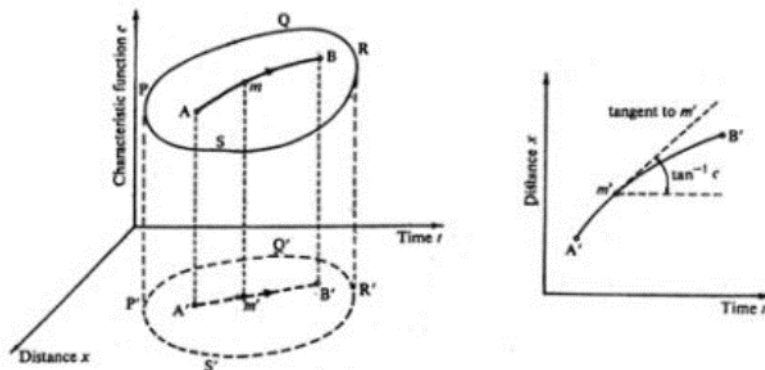


Figure 1. 2: Graphical representation of method of characteristics.

This method for the flow computation is based on the equations written in non-conservative form, as follows:

$$\frac{\partial \rho}{\partial t} + \frac{\partial}{\partial x}(\rho u) + \frac{\rho u}{F} \frac{dF}{dx} = 0 \quad (1.3)$$

$$\frac{\partial u}{\partial t} + u \frac{\partial u}{\partial x} + \frac{1}{\rho} \frac{\partial p}{\partial x} + G = 0 \quad (1.10)$$

$$\left(\frac{\partial p}{\partial t} + u \frac{\partial p}{\partial x} \right) - a^2 \left(\frac{\partial \rho}{\partial t} + u \frac{\partial \rho}{\partial x} \right) - \rho(k-1) \left(\frac{\partial q}{\partial t} - \frac{\Delta H_{react}}{\rho} + uG \right) = 0 \quad (1.22)$$

Combining linearly the three equations it is possible to write them in a form that explicits the three quantities $(u+a), (u-a), u$.

$$\begin{aligned} \left(\frac{\partial p}{\partial t} + (u+a) \frac{\partial p}{\partial x} \right) + \rho a \left(\frac{\partial u}{\partial t} + (u+a) \frac{\partial u}{\partial x} \right) - (k-1)(\rho q - \Delta H_{react} + uG) \\ + a^2 \frac{\rho u}{F} \frac{dF}{dx} + \rho a G = 0 \end{aligned} \quad (1.33)$$

$$\begin{aligned} \left(\frac{\partial p}{\partial t} + (u-a) \frac{\partial p}{\partial x} \right) - \rho a \left(\frac{\partial u}{\partial t} + (u-a) \frac{\partial u}{\partial x} \right) - (k-1)(\rho q - \Delta H_{react} + uG) \\ + a^2 \frac{\rho u}{F} \frac{dF}{dx} - \rho a G = 0 \end{aligned} \quad (1.34)$$

$$\left(\frac{\partial p}{\partial t} + u \frac{\partial p}{\partial x} \right) - a^2 \left(\frac{\partial \rho}{\partial t} + u \frac{\partial \rho}{\partial x} \right) - (k-1)(\rho q - \Delta H_{react} + \rho u G) = 0 \quad (1.35)$$

Then, the equations can be simplified assuming the following ‘‘source terms’’:

$$\Delta_1 = -(k-1)(\rho q - \Delta H_{react} + \rho u G) \quad (1.36)$$

$$\Delta_2 = a^2 \frac{\rho u}{F} \frac{dF}{dx} \quad (1.37)$$

$$\Delta_3 = \rho a G \quad (1.38)$$

The first and third term are dissipative, so we assume a value higher than zero only in the case of ‘‘non-homentropic flow’’, so considering friction and heat exchange at the border of the ducts, whereas the second one is conservative because it takes into account only the cross-section variation of the ducts.

Now, the ‘‘compact form’’ of the system is the following:

$$\left(\frac{\partial p}{\partial t} + (u+a) \frac{\partial p}{\partial x} \right) + \rho a \left(\frac{\partial u}{\partial t} + (u+a) \frac{\partial u}{\partial x} \right) + \Delta_1 + \Delta_2 + \Delta_3 = 0 \quad (1.39)$$

$$\left(\frac{\partial p}{\partial t} + (u-a) \frac{\partial p}{\partial x} \right) - \rho a \left(\frac{\partial u}{\partial t} + (u-a) \frac{\partial u}{\partial x} \right) + \Delta_1 + \Delta_2 + \Delta_3 = 0 \quad (1.40)$$

$$\left(\frac{\partial p}{\partial t} + u \frac{\partial p}{\partial x}\right) - a^2 \left(\frac{\partial \rho}{\partial t} + u \frac{\partial \rho}{\partial x}\right) + \Delta_1 = 0 \quad (1.41)$$

If the computational process happens on the characteristic lines in the plane (x,t), the terms in brackets will become ordinary derivatives with properties dependent on the flow ones.

As an example, for the wave propagation velocity into the flow, defined as $u+a$, the following relationship is valid:

$$\frac{\partial p(x(t), t)}{\partial t} = \left(\frac{\partial p}{\partial t} + \frac{\partial p}{\partial x} \frac{\partial x}{\partial t}\right) = \left(\frac{\partial p}{\partial t} + (u + a) \frac{\partial p}{\partial x}\right) \quad (1.42)$$

So, the equations that will define the characteristic lines used for transforming the partial derivatives will be the following, that are continuous in the (x,t) plan, called “direction equations”:

$$\frac{dx}{dt} = u + a, \text{ absolute velocity of a progressive wave} \quad (1.43)$$

$$\frac{dx}{dt} = u - a, \text{ absolute velocity of a regressive wave} \quad (1.44)$$

$$\frac{dx}{dt} = u, \text{ flow line velocity} \quad (1.45)$$

The characteristic lines into the plan are the one that can be graphically represented as shown in figure 1.3, where are written on a discretized (x,t) plan: every characteristic line represents a separation between two different regions of the plan, where we have a discontinuity into the derivated variables but not into the fluid-dynamic ones.

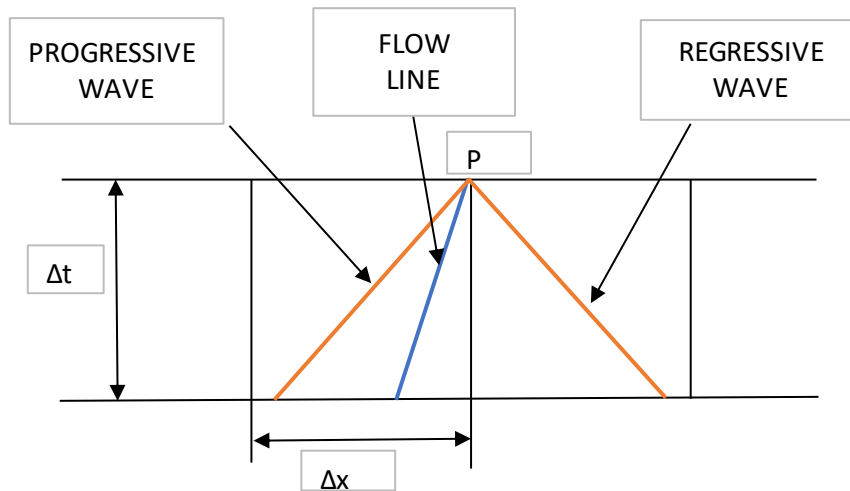


Figure 1. 3: characteristic lines drawn into the discretized (x,t) space

The equations of the system, written on the characteristic lines and so transformed into ordinary derivative ones, are called “compatibility equations”, as follows:

$$\frac{dp}{dt} + \rho a \frac{du}{dt} + \Delta_1 + \Delta_2 + \Delta_3 = 0 \quad (1.46)$$

$$\frac{dp}{dt} - \rho a \frac{du}{dt} + \Delta_1 + \Delta_2 - \Delta_3 = 0 \quad (1.47)$$

$$\frac{dp}{dt} - a^2 \frac{d\rho}{dt} + \Delta_1 = 0 \quad (1.48)$$

In order to understand the mechanism, it can be assumed an homentropic case at constant section, where all the three source terms are none, in order to achieve the following equations:

$$dp + \rho a du = 0 \quad (1.49)$$

$$dp - \rho a du = 0 \quad (1.50)$$

$$dp - a^2 d\rho = 0 \quad (1.51)$$

Since the case is homentropic, the two following relations are feasible:

$$\frac{p}{\rho^k} = \text{constant} \quad (1.52)$$

$$\frac{\rho}{a^{2/(k-1)}} = \text{constant} \quad (1.53)$$

Then, differentiating both, the equations 1.49 and 1.50 can be transformed as follows:

$$du + \frac{2}{k-1} da = 0 \quad (1.54)$$

$$du - \frac{2}{k-1} da = 0 \quad (1.55)$$

Obtaining the differential of the speed of sound with respect to the flow velocity, which is:

$$\frac{da}{du} = -\frac{k-1}{2} \quad (1.56)$$

$$\frac{da}{du} = +\frac{k-1}{2} \quad (1.57)$$

This gives two families of curves, related one to the progressive wave (λ curve) and one to the regressive wave (β curve):

$$\lambda \rightarrow \begin{cases} \frac{dx}{dt} = u + a \\ \frac{da}{du} = -\frac{k-1}{2} \end{cases} \quad \beta \rightarrow \begin{cases} \frac{dx}{dt} = u - a \\ \frac{da}{du} = +\frac{k-1}{2} \end{cases}$$

Both of these curves are representable in appropriate graphs, a “position diagram” where are represented the characteristic curves (first equations of the systems) and a “state diagram” where are represented the differential between sound speed and flow velocity, as shown in figure 1.4:

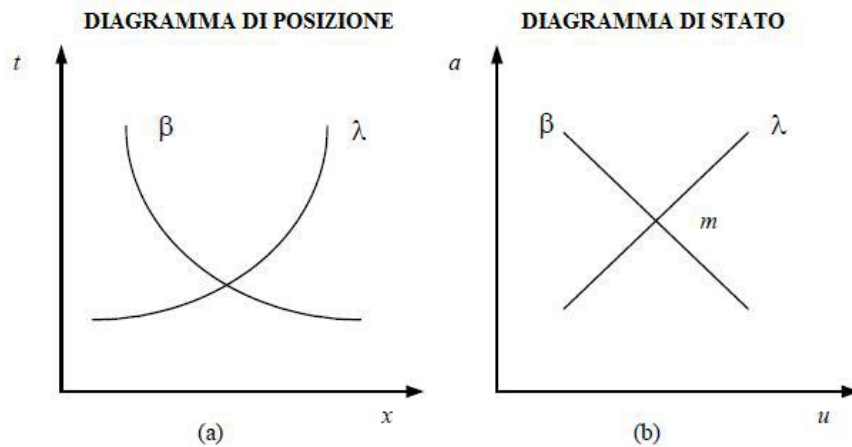


Figure 1. 4: Position and state diagrams for the Riemann variables.

The solution is graphically found in the interception of the two families of curves.

Then, is possible to see how, writing the two equations as:

$$d\left(u + \frac{2}{k-1}a\right) = 0 \quad (1.58)$$

$$d\left(u - \frac{2}{k-1}a\right) = 0 \quad (1.59)$$

The two terms into the brakets are constant, due to the fact that the differential is none. This things is possible if we consider an homentropic flow, where the two values are called “Riemann invariants”, whereas in different case they would vary, and then be named as “Riemann variables”.

Riemann invariants

$$J_+ = u + \frac{2}{k-1}a \quad (1.60)$$

$$J_- = u - \frac{2}{k-1}a \quad (1.61)$$

This is finally the correct equation set used by this method.

As a last thing, it is used to adimensionalize all the variables, in order to define the one that will be used into the proper computational process:

$$A = \frac{a}{a_{ref}}, \text{ non - dimensional speed of sound} \quad (1.62)$$

$$U = \frac{u}{u_{ref}}, \text{ non - dimensional flow velocity} \quad (1.63)$$

$$A_A = \frac{a_A}{a_{ref}}, \text{ non - dimensional "entropic speed of sound"} \quad (1.64)$$

$$Z = \frac{a_{ref}t}{x_{ref}}, \text{ non - dimensional time} \quad (1.65)$$

$$X = \frac{x}{x_{ref}}, \text{ non - dimensional spatial coordinate} \quad (1.66)$$

The reference values are chosen using "opportune points" for the computational process, that phisically are better explicable looking at the figure 1.5:

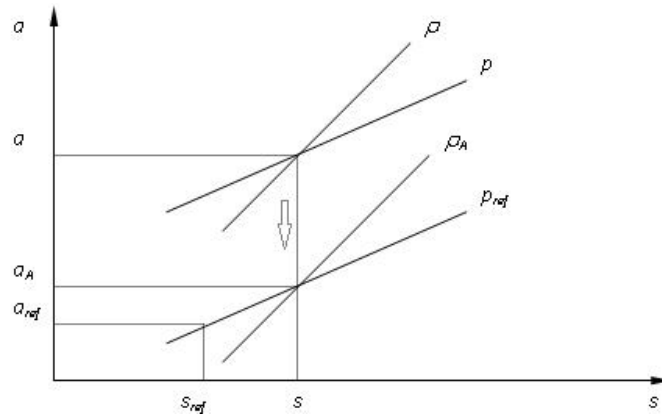


Figure 1. 5: a/s diagram for recognizing the value of a_{ref} .

It is possible to see that the value of a_A is the homentropic speed of sound taken at a different level of pressure, so applying an homentropic compression or expansion: due to the propriaties of the transformatio, the two following relations are considered valid:

$$\frac{p}{p_{ref}} = \left(\frac{a}{a_A} \right)^{\frac{2k}{k-1}} \quad (1.67)$$

$$\frac{\rho}{\rho_A} = \left(\frac{p}{p_{ref}} \right)^{\frac{1}{k}} \quad (1.68)$$

In a non-homentropic case the speed of sound will be related to the local enthalpy, which is generally different with respect to the reference one: this has to be taken in account, considering the isobaric enthalpy variation:

$$ds|_p = \frac{dh}{T} = C_p \frac{dh}{h} \quad (1.69)$$

Then, considering that the enthalpy and its variation can be written as a function of the speed of sound in the following way:

$$h = C_p T = \frac{kRT}{k-1} = \frac{k}{k-1} \frac{p}{\rho} = \frac{a^2}{k-1} \quad (1.70)$$

$$\frac{dh}{h} = \frac{2da}{a} \quad (1.71)$$

It is possible to relate the enthalpy and the speed of sound:

$$ds|_p = 2C_p \frac{da}{a} \quad (1.72)$$

And so, in a non-homentropic case, the relationship between enthalpy and speed of sound can be written in a non-dimensional form as:

$$A_A = \frac{a_A}{a_{ref}} = e^{\frac{(s-s_{ref})}{2C_p}} \quad (1.73)$$

Finally, it can be introduced the Riemann invariants:

$$\lambda = A + \frac{k-1}{2} U, \text{ constant along } \left(\frac{dX}{dZ} \right) = U + A \quad (1.74)$$

$$\beta = A - \frac{k-1}{2} U, \text{ constant along } \left(\frac{dX}{dZ} \right) = U - A \quad (1.75)$$

That are constant in the case of homentropic flow, and then assume value different from zero in the opposite case, becoming Riemann variables which variation is the following:

$$d\lambda = dA + \frac{k-1}{2} dU \quad (1.76)$$

$$d\beta = dA - \frac{k-1}{2} dU \quad (1.77)$$

Thanks to compatibility equations, is possible to evaluate these variations as follows:

λ -characteristic (progressive wave)

Direction equation:

$$\left(\frac{dX}{dZ}\right) = U + A \quad (1.78)$$

Compatibility equation:

$$d\lambda = -\frac{(k-1)(AU)}{2} \left(\frac{1}{F} \frac{df}{dX}\right) dz - \frac{(k-1)}{2} \frac{2x_{ref}}{D} U^2 \frac{U}{|U|} \left[1 - (k-1) \frac{U}{A}\right] dZ + \frac{(k-1)^2}{2} \frac{qx_{ref}}{a^3_{ref}} \frac{1}{A} dZ + \frac{A}{A_A} dA_A \quad (1.79)$$

β -characteristic (progressive wave)

Direction equation:

$$\left(\frac{dX}{dZ}\right) = U - A \quad (1.80)$$

Compatibility equation:

$$d\beta = -\frac{(k-1)(AU)}{2} \left(\frac{1}{F} \frac{df}{dX}\right) dz + \frac{(k-1)}{2} \frac{2x_{ref}}{D} U^2 \frac{U}{|U|} \left[1 - (k-1) \frac{U}{A}\right] dZ + \frac{(k-1)^2}{2} \frac{qx_{ref}}{a^3_{ref}} \frac{1}{A} dZ + \frac{A}{A_A} dA_A \quad (1.81)$$

Path line

Direction equation:

$$\left(\frac{dX}{dZ}\right) = U \quad (1.82)$$

Compatibility equation:

$$dA_A = -\frac{(k-1)}{2} \frac{A_A}{A^2} dZ \left(\frac{2x_{ref}}{D} |U^3| + \frac{qx_{ref}}{a^3_{ref}}\right) dZ \quad (1.83)$$

Hence, observing the first two compatibility equations, it is possible to see that the variation of the Riemann variables is due to four phenomena:

$$d(\lambda, \beta) = \delta_{setion} + \delta_{friction} + \delta_{heat\ exchange} + \delta_{entropy} \quad (1.84)$$

In the third one the entropy variation that makes the problem non-homentropic is due only to two components:

$$d(\lambda, \beta) = \delta_{friction} + \delta_{heat\ exchange} \quad (1.85)$$

Considering now the physical meaning of the method of characteristics, it's known that into a flow the conditions are given by the mass transportation and the pressure perturbations that travel into the ducts at the speed of sound.

In a section i of the duct, at the time $t + \Delta t$, the conditions in a certain point called P are due only to the gas states at the previous time t , so from the points C,D,F, as shown in figure 1.6:

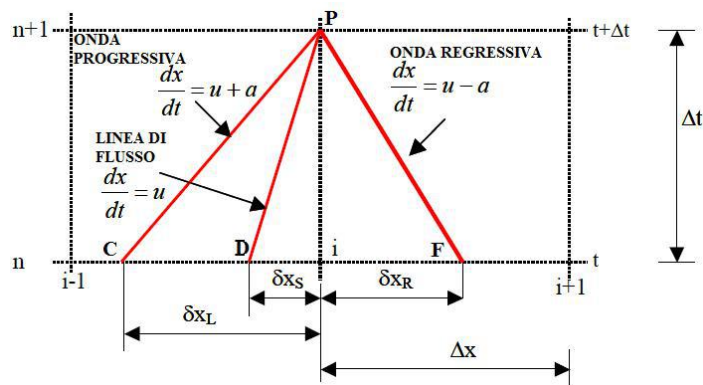


Figure 1. 6: the effects on a point P due to the previous conditions in C,D,F

It is possible to see that the red lines are the characteristic lines, with slope is dependent from the speed of sound due to the relation given in the direction equations.

Now, the method works in the following way: when the values of the Riemann variables at the time Z (because it is non-dimensional) are known, it is possible to find the entropy variation using the equation 1.83 (path line).

Then, since the entropy variation is known, the compatibility equation 1.79 and 1.81 are used to find the Riemann variables variations through the characteristic lines, in order to compute their new value at the time $Z + \Delta Z$, because:

$$\lambda_{Z+\Delta Z} = \lambda + \Delta\lambda \quad (1.86)$$

$$\beta_{Z+\Delta Z} = \beta + \Delta\beta \quad (1.87)$$

Finally, inverting the equations 1.74 and 1.75 is possible to find the solution:

$$A = \frac{\lambda + \beta}{2} \quad (1.88)$$

$$U = \frac{\lambda - \beta}{k - 1} \quad (1.89)$$

Since this method has to be applied by a computer, it is important to improve a numeric approximated method, called “mesh method of characteristics”.

In this method all the points of intersection of the characteristic lines are defined in the (x,t) plan, such to create a discrete mesh of spatial and temporal positions.

The discretisation happens differently on the two axes:

- Space: this domain is discretized considering the number of sub-elements in which the duct is divided: if there are l subelements, there will be $l+1$ knots. The number of subelements is often chosen as a trade-off between accuracy of the solution and computational effort.
- Time: this domain is discretized following the Courant-Friedrichs-Lewy criterion of stability: considering the maximum wave speed propagation $u+a$, the criterion says that the time step has to be enough short that the wave cannot travel an entire spatial step.

More practically, introducing the CFL number, it has to be:

$$CFL = (a + |u|) \frac{\Delta t}{\Delta x} \leq 1 \quad (1.90a)$$

$$CFL = (A + |U|) \frac{\Delta Z}{\Delta X} \leq 1 \quad (1.90b)$$

So, in order to have all the knots of the point $Z+\Delta Z$ in the right domain, the CFL number has to be lower than one.

In this mesh method, the computation of the Riemann values for every time step happens only in the spatial knots, in a way represented in figure 1.7:

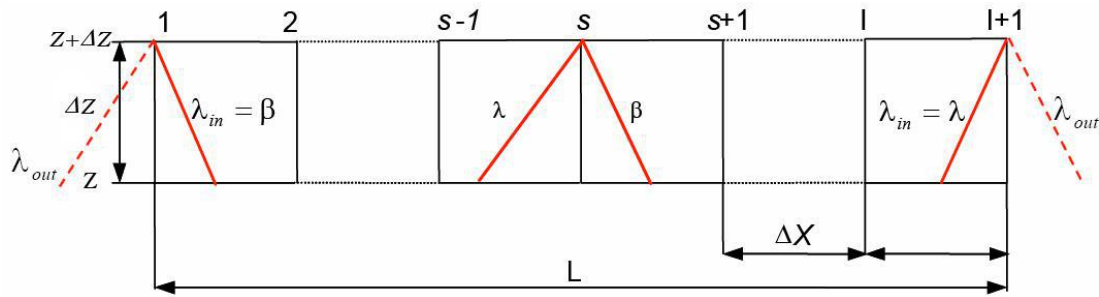


Figure 1. 7: example of computational process in a space/time grid

In order to simplify the computing procedure, acting in a more general way, the two Riemann variables are renamed as λ_I, λ_{II} .

At the adimensional time Z , known the three variables $\lambda_I, \lambda_{II}, A_A$, the time step is computed using the CFL criterion.

Then, the characteristic lines are designed going backwards, so starting from every knot at the time $Z+\Delta Z$ and going to time Z , as shown in figure 1.8:

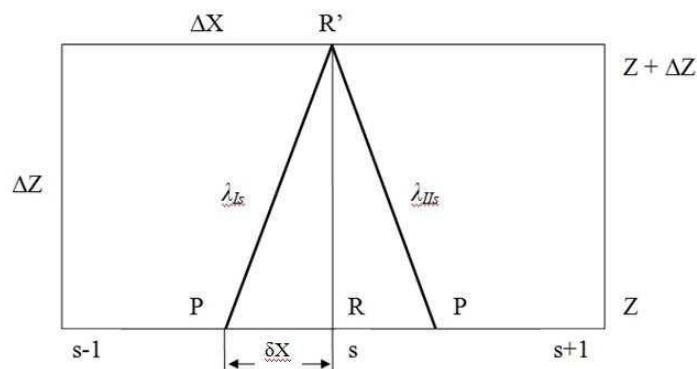


Figure 1. 8: design of the characteristic lines. The path line is the central one, that intersecates the time Z axis in the point s .

The slope of the lines in the graph is constant, whereas in reali it is not: this is so an approximation, and the error introduced is smaller the more the grid is close.

The position of the points P can be computed starting from the values of the two Riemann variables, in the following way (as an example, it is shown the process for the point at the left, but it's the same for the other):

$$\frac{\delta X_L}{\Delta Z} = U_L + A_L \quad (1.91)$$

Then, using the equations 1.88, 1.89 it is possible to obtain:

$$\frac{\delta X_L}{\Delta Z} = a\lambda_{iL} + b\lambda_{iIL} \quad (1.92)$$

Where a , b , are two constant that depend from the gas nature:

$$a = \frac{k+1}{2(k-1)} \quad (1.93)$$

$$b = \frac{3-1}{2(k-1)} \quad (1.94)$$

Now, λ_I is computed by a linear interpolation using the values of λ in the knots i and $i-1$, and similarly λ_{II} :

$$\lambda_{iL} = \lambda_{i-} - \frac{\delta X_L}{\Delta X} (\lambda_{ii} - \lambda_{i-1}) \quad (1.95)$$

$$\lambda_{iIL} = \lambda_{iII-} - \frac{\delta X_L}{\Delta X} (\lambda_{iII} - \lambda_{iII-1}) \quad (1.96)$$

And so obtaining the value in function of the interpolated values:

$$\frac{\delta X_L}{\Delta Z} = \frac{a\lambda_{iL} + b\lambda_{iIL}}{\frac{\Delta X}{\Delta Z} + a(\lambda_{ii} - \lambda_{i-1}) - b(\lambda_{iII} - \lambda_{iII-1})} \quad (1.97)$$

Once the Riemann variables are known, it is necessary to evaluate the entropy variation: as provided by the method this is made using the path line compatibility equation, computing the necessary values as an interpolation with the next points, with the generic formula:

$$G_s = G_{i-} - \frac{\delta X_s}{\Delta X} (G_i - G_{i-1}) \quad (1.98)$$

With:

$$\frac{\delta X_s}{\Delta X} = \frac{\lambda_{ii} + \lambda_{iII}}{\frac{\Delta X}{\Delta Z} (k+1) + (\lambda_{ii} - \lambda_{i-1}) - (\lambda_{iII} - \lambda_{iII-1})} \quad (1.99)$$

When the values of A_{AS} , dA_{AS} are known, it is possible to compute the entropy of point P using the relation:

$$A_{AP} = A_{AS} + dA_{AS} \quad (1.100)$$

Then, the entropy variation along the characteristic line is:

$$dA_{AL} = A_{AP} - A_{AL} \quad (1.101)$$

Finally, inserting these two values into the equations 1.79 and 1.81, the compatibility equations of the waves, allows to compute the variations $\Delta\lambda$ and $\Delta\beta$, that leads to the evaluation of all the other proprieties.

This method allows to compute the proprieties in all the points of the mesh apart from the first and the last: for the evaluation of the missing Riemann variable are used the border conditions, assumin them in a quasi-steady state that is represented by an algebric equation, so without any derivative term.

Nowadays this method is used only for modeling the border zones.

1.2.2 Shock capturing methods

After the '80s of the past century, new and more precise and robut methods for computing the gas flows have been implemented, in order to avoid the problems of low accuracy that affect the method of characteristics.

These methods are so called due to their capacity to relive the discontinuities into the solution that are given by shockwaves, chemical composition changes and so, and they are based on symmetrical finite differences.

The main problem of these methods come from the fact that they have a "II order of accuracy", wich brings back the presence of *spurious oscillations* into the solution that have to be dumped with proper algorithms.

All the most important methods are applied on the hyperbolic system written in the conservative matricial form, the one described in the equation 1.26.

As an example it could be considered an homentropic case, where the systems becomes as follows:

$$\frac{\partial \bar{w}(x, t)}{\partial t} + \frac{\partial \bar{F}(\bar{w})}{\partial x} = 0 \quad (1.102)$$

Then, the Gauss theorem can be applied on the integrated version:

$$\int_t^{t+\Delta t} \int_x^{x+\Delta x} \left(\frac{\partial \bar{w}(x, t)}{\partial t} + \frac{\partial \bar{F}(\bar{w})}{\partial x} \right) dxdt = 0 \quad (1.103)$$

Since the computational process passes through a numerical approximation, the vector will be “splitted” on all the points of the mesh of the (x,t) grid:

$$\bar{W}(x, t) \cong \bar{W}_i^n(i\Delta x, n\Delta t) \quad (1.104)$$

Such that the equation 1.103 becomes:

$$(\bar{W}_i^{n+1} - \bar{W}_i^n)\Delta x + \left(\bar{F}_{i+\frac{1}{2}}^n - \bar{F}_{i-\frac{1}{2}}^n \right) \Delta t = 0 \quad (1.105)$$

Where the terms are an average on, respectively, space and time:

$$\bar{W}_i = \frac{1}{\Delta x} \int_{x_{i-1/2}}^{x_{i+1/2}} \bar{W} dx; \bar{F}_{i\pm 1/2} = \frac{1}{\Delta t} \int_{t^n}^{t^{n+1}} \bar{F} dt \quad (1.106)$$

The use of the integral average allows to treat discontinuities even without knowing before their precise position.

It's evident that the equation 1.105 can be written event in the following form:

$$\frac{(\bar{W}_i^{n+1} - \bar{W}_i^n)}{\Delta t} + \frac{\left(\bar{F}_{i+\frac{1}{2}}^n - \bar{F}_{i-\frac{1}{2}}^n \right)}{\Delta x} = 0 \quad (1.107)$$

In this way it's possible to do a sum along x and find:

$$\Delta x \sum_{imin}^{imax} \bar{W}_i^{n+1} = \Delta x \sum_{imin}^{imax} \bar{W}_i^n + \Delta t \left[\bar{F}_{imin+\frac{1}{2}}^n - \bar{F}_{imax-\frac{1}{2}}^n \right] \quad (1.108)$$

Where:

- The first member is the vector W, so the total mass, momentum and energy, at the following time $n+1$;
- The first term of the second member is the same vector but at the time n ;
- The second term is the flow of the conserved quantities through the duct sides.

The validity of the integral proprieties is due to the conservative scheme adopted.

1.2.3 Lax-Wendroff method

It is based on the Taylor expansion of the vector W, and it's possible to use it in two different forms: *single step* or *two step*.

One step method:

Considering an homentropic case, governed by the equation (1.102), it is possible to write it as:

$$\frac{\partial \bar{w}(x, t)}{\partial t} + \frac{\partial \bar{F}(\bar{w})}{\partial \bar{w}} \frac{\partial \bar{w}}{\partial x} = 0 \quad (1.109)$$

Where the *Jacobian matrix* A is represented by the first part of the second term:

$$A = \frac{\partial \bar{F}(\bar{w})}{\partial \bar{w}} \quad (1.110)$$

And its components are expressed as:

$$a_{ij} = \frac{\partial F_i}{\partial W_j} \quad (1.111)$$

The equation so can be written even in the following simplified way:

$$\frac{\partial \bar{w}(x, t)}{\partial t} + A \frac{\partial \bar{w}}{\partial x} = 0 \quad (1.112)$$

Now, the method requires a Taylor expansion of the vector W in the discretized domain, which in the knot i is the following:

$$\bar{w}_i^{n+1} = \bar{w}_i^n + \left. \frac{\partial \bar{w}}{\partial t} \right|_i \Delta t + \frac{1}{2!} \left. \frac{\partial^2 \bar{w}}{\partial t^2} \right|_i \Delta t^2 + O(\Delta t^3) \quad (1.113)$$

Since it is possible to write:

$$\frac{\partial \bar{w}(x, t)}{\partial t} = - \frac{\partial \bar{F}(\bar{w})}{\partial x} = -A \frac{\partial \bar{w}}{\partial x} \quad (1.114)$$

The second derivative into the equation 1.113 can be rewritten as:

$$\frac{\partial^2 \bar{w}}{\partial t^2} = - \frac{\partial}{\partial t} \left(\frac{\partial \bar{F}}{\partial x} \right) = - \frac{\partial}{\partial x} \left(\frac{\partial \bar{F}}{\partial t} \right) \quad (1.115)$$

So, after some substitutions:

$$\frac{\partial \bar{F}}{\partial t} = \frac{\partial \bar{F}}{\partial \bar{w}} \left(\frac{\partial \bar{w}}{\partial t} \right) = \frac{\partial \bar{F}}{\partial \bar{w}} \left(- \frac{\partial \bar{F}}{\partial x} \right) = \frac{\partial \bar{F}}{\partial \bar{w}} \left(-A \frac{\partial \bar{w}}{\partial x} \right) = \left(-A \frac{\partial \bar{F}}{\partial x} \right) \quad (1.116)$$

Finally, the equation 1.115 becomes:

$$\frac{\partial^2 \bar{w}}{\partial t^2} = A \frac{\partial}{\partial x} \left(\frac{\partial \bar{F}}{\partial x} \right) \quad (1.117)$$

Now, the relationship found can allow to write the equation 1.113 as an expansion of spatial differences, thanks to the Jacobian matrix:

$$\bar{w}_i^{n+1} = \bar{w}_i^n - A \left. \frac{\partial \bar{w}}{\partial x} \right|_i^n \Delta t + \frac{1}{2!} \frac{\partial}{\partial x} \left(A^2 \frac{\partial \bar{w}}{\partial x} \right) \Big|_i^n \Delta t^2 + O(\Delta t^3) \quad (1.118a)$$

$$\bar{w}_i^{n+1} = \bar{w}_i^n - \left. \frac{\partial \bar{F}}{\partial x} \right|_i^n \Delta t + \frac{1}{2!} \frac{\partial}{\partial x} \left(A \frac{\partial \bar{F}}{\partial x} \right) \Big|_i^n \Delta t^2 + O(\Delta t^3) \quad (1.118b)$$

Then, the derivatives can be substitute with *centered finite differences*, passing into a discrete dominion, obtaining the one step Lax-Wendroff expressions:

$$\bar{w}_i^{n+1} = \bar{w}_i^n - A \left(\frac{\bar{w}_{i+1}^n - \bar{w}_{i-1}^n}{2\Delta x} \right) \Delta t + \frac{A^2}{2!} \left(\frac{\bar{w}_{i+1}^n - 2\bar{w}_i^n + \bar{w}_{i-1}^n}{\Delta x^2} \right) \Delta t^2 \Delta \quad (1.119a)$$

$$\begin{aligned} \bar{w}_i^{n+1} = \bar{w}_i^n - \frac{\Delta t}{2\Delta x^2} (\bar{F}_{i+1}^n - \bar{F}_{i-1}^n) \Delta t + \frac{\Delta t^2}{2\Delta x^2} (A_{i+\frac{1}{2}}^n (\bar{F}_{i+1}^n - \bar{F}_i^n) \\ - A_{i-\frac{1}{2}}^n (\bar{F}_i^n - \bar{F}_{i-1}^n)) \end{aligned} \quad (1.119b)$$

Where the 1.119a is usable when A is constant, and the 1.119b is for the case when A is not constant.

In that situation the values for the jacobian matrix are:

$$A_{i\pm 1/2}^n = \frac{1}{2} (A_i^n + A_{i\pm 1}^n) \quad (1.120a)$$

$$A_{i\pm 1/2}^n = A(W_i^n + W_{i\pm 1}^n) \quad (1.120b)$$

Whereas this method can be really accurate, it's not really used due to the high computational effort requested for computing the jacobian matrix into every knot.

Two step method:

This method allow to not compute the jacobian matrix, using an intermediate computation of the solution vector W, as shown in figure 1.9:

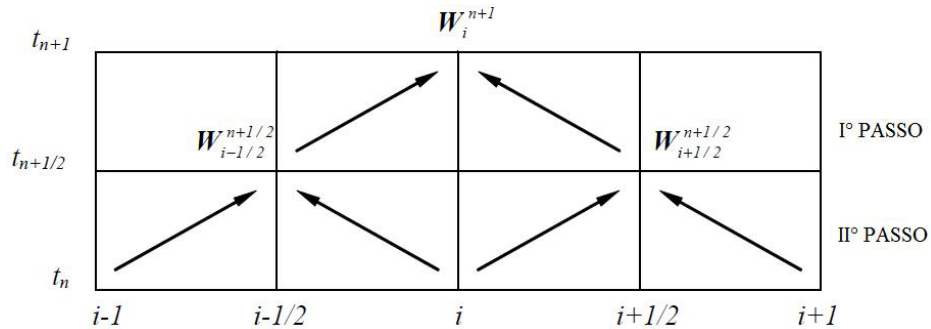


Figure 1. 9: two-step Lax-Wendroff method computational scheme

- I step: once the vectors W , F are known into the knot i , the previous and the following one, the vector W in the intermediate time $n+1/2$ is found by a Taylor expansion using finite difference:

$$\bar{w}_{i+1/2}^{n+1/2} = \left(\frac{\bar{w}_{i+1}^n - \bar{w}_i^n}{2} \right) - \left(\frac{\bar{F}_{i+1}^n - \bar{F}_i^n}{2\Delta x} \right) \Delta t \quad (1.121a)$$

$$\bar{w}_{i-1/2}^{n+1/2} = \left(\frac{\bar{w}_i^n - \bar{w}_{i-1/2}^n}{2} \right) - \left(\frac{\bar{F}_i^n - \bar{F}_{i-1}^n}{2\Delta x} \right) \Delta t \quad (1.121b)$$

- II step: then, it is possible to compute the flow vector F into the intermediate time, and finally compute the solution vector W at the time $n+1$ in the knot i .

$$\bar{w}_i^{n+1} = \bar{w}_i^n - \left(\frac{\bar{F}_{i+1/2}^{n+1/2} - \bar{F}_{i-1/2}^{n+1/2}}{\Delta x} \right) \Delta t \quad (1.122)$$

The time step is computed using the CFL stability criterium, as the first accuracy order methods.

1.2.4 MacCormack method

It's a two-step method, where the steps are called "predictor" and "corrector".

Considering the homentropic vectorial equation 1.102 as always, assuming a constant-section duct, the two phases are:

- Predictor phase: once the vectors W , F in time n , it can be computed an approximate version of the solution vector at time t^* using forward finite differences:

$$\left(\frac{\bar{w}_i^* - \bar{w}_i^n}{\Delta t} \right) - \left(\frac{\bar{F}_{i+1}^n - \bar{F}_i^n}{\Delta x} \right) = 0 \quad (1.123a)$$

$$\bar{w}_i^* = \bar{w}_i^n - \frac{\Delta t}{\Delta x} (\bar{F}_{i+1}^n - \bar{F}_i^n) \quad (1.123b)$$

Then, even the vector F^* can be computed.

The value of the solution vector into an intermediate time step $n+1/2$ can be computed as an average between the estimated value W^* and the previous W_i^n .

$$\bar{w}_i^{n+1/2} = -\frac{1}{2} (\bar{w}_i^* + \bar{w}_i^n) \quad (1.124)$$

- Corrector phase: concluding the time step by going ahead a time $\Delta t/2$, a finite backwards difference allows to find the final solution:

$$\bar{w}_i^{n+1} = \bar{w}_i^{n+1/2} - \frac{\Delta t}{2} \left(\frac{\bar{F}_i^* - \bar{F}_{i-1}^*}{\Delta x} \right) \quad (1.125)$$

The whole mechanism is shown in figure 1.10:

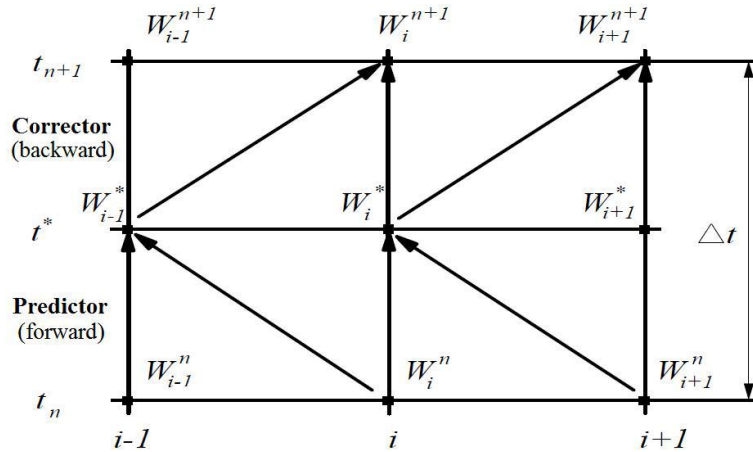


Figure 1. 10: MacCormack forward predictor-backward corrector computational scheme

It is important to remind that the method can be implemented even in the opposite way (backward predictor-forward corrector), but the results will be a little different.

The best way usually is to follow the discontinuity propagation into the *predictor* phase, whereas when the direction is unknown a good trade off is to invert the scheme at every step.

The time-step length is still given by the CFL stability criterion.

1.2.5 Spurious oscillations problem

The second accuracy order methods, according with the Godunov theorem, have the problem of a presence of numerical oscillations across the discontinuities of the solution.

In fact, every numerical method above the first accuracy order that can be resumed with the following scheme:

$$\bar{w}_i^{n+1} = \sum_k c_k \bar{w}_{i+k}^n \quad (1.126)$$

Presents the problem of an oscillating solution, which has no physical sense.

The sufficient and necessary conditions that a method should have to avoid these oscillations are given by the Hartem criterion: defining the total variation of a solution vector as:

$$TV(\bar{w}_i^n) = \sum_k |\bar{w}_{i+1}^n - \bar{w}_i^n| \quad (1.127)$$

If, going on through the time steps the total variation do not increase, the spurious oscillations problem will be absent:

$$TV(\bar{w}_i^{n+1}) \leq TV(\bar{w}_i^n) \quad (1.128)$$

These methods are known as “total variation diminishing”, whereas the two last observed are not into this category.

It is possible to bring them into this category using some damping systems that can modify the c_k coefficients, in order to make them dependent from the solution W .

These damping systems can be:

- Pre-processing, if the data are modified before the solution, so step by step;
- Post-processing, if the solution is corrected after all the time steps.

The two systems used by *Gasdyn* are in the second category, and are:

- FCT technique;
- Flux limiters.

FCT technique:

This technique has been introduced in 1973 by Boris and Book, and is constituted by three stages:

- Transport stage, which is the one where the solution is obtained by a second order method, represented by the transport operator T :

$$\bar{w}_i^{n+1} = \bar{w}_i^n + T(\bar{w}_i^n) \quad (1.129)$$

- Diffusion stage, where a numerical diffusion is introduced in order to damp any non-physical oscillation by a flux θ :

$$\bar{\theta}(\bar{w}_{i+1/2}) = \frac{1}{8}(\bar{w}_{i+1} - \bar{w}_i) \quad (1.130a)$$

$$\bar{\theta}(\bar{w}_{i-1/2}) = \frac{1}{8}(\bar{w}_i - \bar{w}_{i-1}) \quad (1.130b)$$

At which corresponds the diffusion D_i :

$$D_i = \bar{\theta}(\bar{w}_{i+1/2}) - \bar{\theta}(\bar{w}_{i-1/2}) \quad (1.131)$$

Then, there are two possible ways to follow in order to achieve the final value of the solution vector:

1. Damping diffusion, if for the computation of the diffusion factor it is used the vector at time n :

$$\bar{w}_D^{n+1} = \bar{w}_i^{n+1} + D(\bar{w}_i^n) \quad (1.132)$$

2. Smoothing diffusion, if the diffusion factor is computed using the solution vector at the new time $n+1$:

$$\bar{w}_D^{n+1} = \bar{w}_i^{n+1} + D(\bar{w}_i^{n+1}) \quad (1.133)$$

- Anti-diffusion stage, where a counter-diffusive non-linear operator A is introduced in order to remove the diffusion effects where unnecessary:

$$A(\bar{w}_i^{n+1}) = -\bar{\Psi}(\bar{w}_{i+1/2}^{n+1}) + \bar{\Psi}(\bar{w}_{i-1/2}^{n+1}) \quad (1.134)$$

Where the flux limiter $\bar{\psi}$ is defined using the Ikeda-Nakagawa proposal:

$$\bar{\Psi}(\bar{w}_i^{n+1}) = \bar{s} \cdot \max \left(0, \min \left(\frac{5}{8} \bar{s} \Delta \bar{w}_{i+1/2}^{n+1}, \frac{1}{8} \Delta \bar{w}_{i+1/2}^{n+1}, \frac{5}{8} \bar{s} \Delta \bar{w}_{i+3/2}^{n+1} \right) \right) \quad (1.134)$$

Where:

$$\bar{s} = \text{sgn}(\Delta \bar{w}_{i+1/2}^{n+1}) \quad (1.135)$$

$$\Delta \bar{w}_{i+1/2}^{n+1} = \bar{w}_{i+1}^{n+1} - \bar{w}_i^{n+1} \quad (1.136)$$

$$\Delta \bar{w}_{i-1/2}^{n+1} = \bar{w}_i^{n+1} - \bar{w}_{i-1}^{n+1} \quad (1.137)$$

$$\Delta \bar{w}_{i+3/2}^{n+1} = \bar{w}_{i+2}^{n+1} - \bar{w}_{i+1}^{n+1} \quad (1.138)$$

There are finally two possible values of the damped solution, depending on the strategy followed:

- Damping case:

$$\bar{w}_{DA}^{n+1} = \bar{w}_D^{n+1} + A(\bar{w}_i^n) \quad (1.139)$$

- Smoothing case:

$$\bar{w}_{DA}^{n+1} = \bar{w}_D^{n+1} + A(\bar{w}_i^{n+1}) \quad (1.140)$$

The difference between this two possibilities is that the damping is more effective in reducing the spurious oscillations, but makes the numerical process become unstable, whereas the smoothing can maintain the process stable but has lower reduction effect on the oscillation.

A way for limiting the instabilities is to reduce the temporal step length, so imposing that the CFL has to be lower than 0.866 instead of 1, which brings back a higher amount of computational effort.

Flux limiters:

The flux limiters method is based on the idea of applying the diffusion only in the regions where spurious oscillations are present, in order to avoid any non-physical numerical oscillation.

The flux limiter ϕ can control the oscillations and is function of the ratio between successive solution's gradients, defined as:

$$\phi_i = \phi(r_i) \tag{1.141}$$

Where the ratio is:

$$r_i = \frac{\Delta \bar{w}_{i-1/2}^n}{\Delta \bar{w}_{i+1/2}^n} \tag{1.142}$$

$$\Delta \bar{w}_{i+1/2}^n = \Delta \bar{w}_{i+1}^n - \Delta \bar{w}_i^n \tag{1.143}$$

$$\Delta \bar{w}_{i-1/2}^n = \Delta \bar{w}_i^n - \Delta \bar{w}_{i-1}^n \tag{1.144}$$

If the ratio in two adjacent solution is near to one, the second order accuracy is maintained because there are no oscillations, whereas near the discontinuities the solution is degraded into a first accuracy order.

On an hyperbolic system the application can be complex, but as an example it is possible to show this method on a linear partial derivative equation like the following:

$$\frac{\partial w}{\partial t} - a \frac{\partial w}{\partial x} = 0 \tag{1.145}$$

The solution, using the Lax-Wendroff method, is:

$$\bar{w}_i^{n+1} = \bar{w}_i^n + \frac{v}{2} \left(\Delta \bar{w}_{i+1/2}^n + \Delta \bar{w}_{i-1/2}^n \right) + \frac{v^2}{2} \left(\Delta \bar{w}_{i+1/2}^n + \Delta \bar{w}_{i-1/2}^n \right) \tag{1.146}$$

Where v is the CFL.

Applying at this equation a dissipative term in order to have an *artificial viscosity effect* is possible to obtain the TVD propriety for the numerical solution. For example, using a positive constant term it is obtained the following dissipative term:

$$G_{i+1/2}^+(r_i^+) \bar{w}_{i+1/2}^n - G_{i-1/2}^+(r_{i-1}^+) \bar{w}_{i-1/2}^n \quad (1.147)$$

Such that the equation 1.146 becomes:

$$\bar{w}_i^{n+1} = \bar{w}_i^n - \Delta \bar{w}_{i-1/2}^n \left\{ v \left[1 + \frac{1}{2} (1-v) \left(\frac{1}{r_i^+} - 1 \right) \right] - \left[\frac{G_{i+1/2}^+}{r_i^+} - G_{i-1/2}^+ \right] \right\} \quad (1.148)$$

where:

$$r_i = \frac{\Delta \bar{w}_{i-1/2}^n}{\Delta \bar{w}_{i+1/2}^n} \quad (1.149)$$

$$G_{i+1/2}^+(r_i^+) = \frac{v}{2} (1-v) (1 - \varphi(r_i^+)) \quad (1.150)$$

In a case of negative constant, the factors are obtained in a similar way:

$$r_i = \frac{\Delta \bar{w}_{i+1/2}^n}{\Delta \bar{w}_{i-1/2}^n} \quad (1.149)$$

$$G_{i+1/2}^-(r_i^-) = \frac{v}{2} (1-v) (1 - \varphi(r_i^- - 1)) \quad (1.150)$$

Then, the two cases can be combined obtaining the following solution:

$$\begin{aligned} \bar{w}_i^{n+1} = & \bar{w}_i^n + \frac{v}{2} (\bar{w}_{i+1}^n + \bar{w}_{i-1}^n) + \frac{v^2}{2} (\bar{w}_{i+1}^n + 2\bar{w}_i^n + \bar{w}_{i-1}^n) \\ & + [G_{i+1/2}^+(r_i^+) + G_{i+1/2}^-(r_{i+1}^-)] \Delta \bar{w}_{i+1/2}^n \\ & - [G_{i+1/2}^+(r_{i-1}^+) + G_{i+1/2}^-(r_i^-)] \Delta \bar{w}_{i-1/2}^n \end{aligned} \quad (1.151)$$

Where:

$$G_{i+1/2}^+(r_i^+) = \begin{cases} \frac{v}{2} (1-v) (1 - \varphi(r_i^+)) & \text{if } a > 0 \\ 0 & \text{if } a \leq 0 \end{cases} \quad (1.152a)$$

$$G_{i+1/2}^-(r_i^-) = \begin{cases} 0 & \text{if } a > 0 \\ \frac{v}{2} (1-v) (1 - \varphi(r_i^- - 1)) & \text{if } a \leq 0 \end{cases} \quad (1.152b)$$

Since the sign of the coefficient a defines the flow direction, the knowing of that sign is necessary for the solution.

Davis solves this problem using a *non-upwind* scheme defining the G terms as follows:

$$G_{i+1/2}^+(r_i^+) = \frac{|v|}{2}(1 - |v|)(1 - \varphi(r_i^+)) \quad (1.153)$$

$$G_{i+1/2}^-(r_i^-) = \frac{|v|}{2}(1 - |v|)(1 - \varphi(r_i^+)) \quad (1.154)$$

In order to make the method TVD, the flux limiter has to assume certain values, defined into the Davis ammissibility region:

$$\varphi(r) = \begin{cases} 0 & \text{if } r \leq 0 \\ \min(2r, 1) & \text{if } r > 0 \end{cases} \quad (1.155)$$

This brings to a limit on the CFL value, that must be 0.7.

CHAPTER 2: INTRODUCTION AND FUNCTIONING OF GASDYN

2.1 Introduction to GasDyn.

The code used for the simulation of this thesis is GasDyn, which is a 1-D thermo-fluid dynamic simulator that can represent the whole engine functioning in order to achieve all the informations about volumetric efficiency, torque, power, consumption, emissions and combustion of the engine.

This code can take care of the presence of wave effects into the ducts, and deal with all the devices along the gas path such as valves, volumes, turbines and compressors. The schematics of the engine is easily represented into the main window, as shown in figure 2.1:

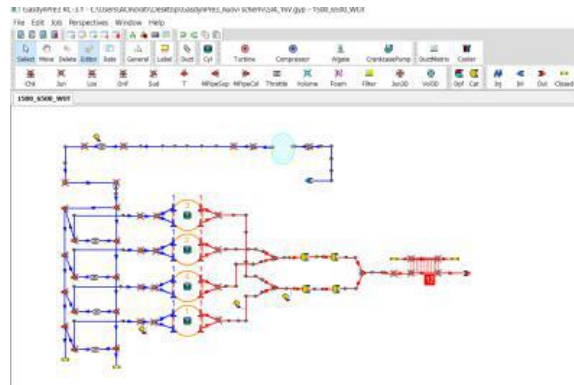


Figure 2.1: GasDyn schematics of a 4 cylinder N/A engine

Inside the cylinders, all the processes are considered using thermodynamic models based on energy conservation equations and mass balance, in the following way.

2.1.1: Instantaneous heat fluxes

The computation of the energy conservation equation needs the evaluation of the instantaneous space averaged heat fluxes, in order to predict the heat transfer between gases and cylinder walls.

There are many sub-models that can describe the process, whereas the most used is the Woschni approach, which includes the effects of radiation into the contribution given by convection, computing the thermal power as follows:

$$q' = h_i(T_g - T_i) \quad (2.1)$$

The value of the convective transfer factor h is found using the relationship within the adimensional numbers for forced convection, which is:

$$Nu = C * Re^{0.8} \quad (2.2)$$

That can be even represented using the variables that constitute the adimensionals:

$$\frac{h_i D}{\lambda} = C * \left(\frac{u \rho D}{\mu} \right)^{0.8} \quad (2.3)$$

Then, assuming the following proportionalities:

$$\lambda \approx T^{0.75} \quad (2.4)$$

$$\rho \approx T^{-1} \quad (2.5)$$

$$\mu \approx T^{0.6} \quad (2.6)$$

And inverting the equation, the following expression is derived:

$$h_i = C * \rho^{0.8} * D^{-0.2} * T^{-0.53} * u^{0.8} \quad (2.7)$$

Since the real values of the local velocity are generally unknown, the model sees the velocity u as sum of two components, the first considering swirl effects by a constant, the second considering the increase of the velocity during the combustion and expansion process, giving the following expression;

$$u = C_2 u_p + C_3 (VT_0)/(p_0)(p - p_{mot}) \quad (2.8)$$

Where the two constant are different depending on the engine phase and the paddle wheel speed ω_s , and p_{mot} is the in-cylinder pressure of the motored engine (the same one but without combustion process).

2.1.2 In-cylinder turbulence

The in-cylinder turbulence has a huge effect on the combustion process, so the code has to take them in account during the computation o the combustion: the main used are the K-k models, wich have this name due to the two variables occurring into the two balance equations: the mean motion kinetic energy K and the turbulenct kinetic energy k .

According to the model, the turbulence is generated as a zero-dimensional energy cascade, because the turbulent kinetic energy is generated from the mean one due to viscous dissipation.

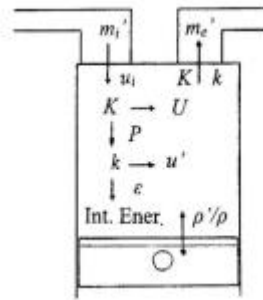


Figure 2.2: zero-dimensional energy cascade

The two balance equations that govern the system of production and dissipation of kinetic energy are the following:

$$\frac{dK}{dt} = m'_i \left(\frac{u_i}{2}\right)^2 - m'_e \left(\frac{u_e}{2}\right)^2 - P - K \left(\frac{m'_e}{m}\right) + k \left(\frac{\rho'}{\rho}\right) \quad (2.9)$$

$$\frac{dk}{dy} = P - \varepsilon - k \left(\frac{m'_e}{m}\right) + k \left(\frac{\rho'}{\rho}\right) \quad (2.10)$$

Where is possible to see that the variation fo kinetic energy is due to:

- Kinetic energy carried by the massflow entering the cylinder;
- Kinetic energy carried outside the cylinder by another massflow;
- Kinetic energy carried by the mass moving into the cylinder;

- Kinetic energy due to the variation of density acted by the in-cylinder processes as compression or combustion.

It is evident that only the mean value is affected by the flow going inside or outside the cylinder, whereas for the turbulent component it is interesting the in-cylinder motion. Since the K-k model is not multidimensional, the kinetic energy variations have to be modeled in a phenomenological way: the factors P and ε so are given by the following relations:

$$P = C_p \left(\frac{K}{\tau_l} \right) \quad (2.11)$$

$$\varepsilon = C_k \left(\frac{K}{\tau'} \right) \quad (2.12)$$

Where C_p , C_k are two model constants, τ_l the integral time scale of large eddies and τ' the time scale of turbulent eddies.

Assuming the turbulence as homogeneous and isotropic, at any time step the two velocity component U (mean component) and u' (mean square root of the velocity fluctuation) are related to the kinetic energy in the following way:

$$K = \frac{1}{2} m U^2 \quad (2.13)$$

$$k = \frac{3}{2} m u'^2 \quad (2.14)$$

The macroscale of turbulence is assumed as a fraction of the representative scale l:

$$l_l = C_{LI} l = \frac{C_{LI} V}{\pi D^2 / 4} \quad (2.15)$$

Where V is the instantaneous value of the cylinder volume and D is the cylinder bore. Once this is known, the time scales are computed as turnover time of the fluid in the relative eddies.

2.2 Spark ignition engines

2.2.1 Cylinder charge model

The spark ignition combustion is modeled using a multi-zone approach, which is made in the following way.

First of all the in-cylinder mixture is divided into burned and unburned zone, which are separated by the flame front, assumed as spherical and infinitesimally thin.

In order to have the satisfaction of the momentum conservation, the pressure is assumed as constant.

Therefore, the solution of the mass and energy conservation equations applied in both zones allow computing the pressure and the temperature in the two zones.

The burnt zone can be also divided in more zones, usually from 2 to 4, of equal mass, and are created during the combustion process, as shown in figure 2.3.

All of these sub-zones do not exchange mass by each other, and are all spherical and centered into the spark plug.

Their chemical composition is computed separately and the same is done with the heat exchange, taking in account the difference of exchanging area of any zone.

This division doesn't affect the thermodynamical data determined by the solution of the conservation equations.

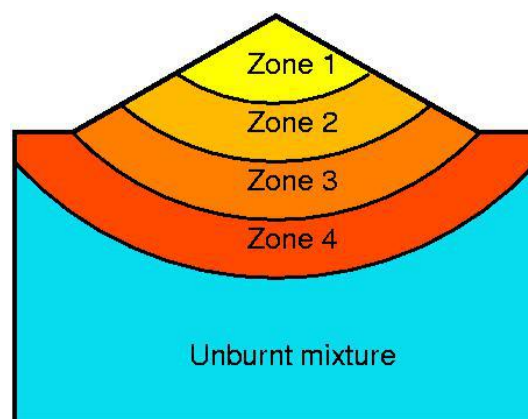


Figure 2. 3: multi-zone approach for spark ignition engines.

There will be two kind of sub-zones: burnt ones and the burning one, which contains the flame front.

The two zones are described by different equations as follows:

- Burned zone: the energy conservation for this kind of zone is:

$$\frac{dH_z}{d\theta} = \frac{dQ_{w,z}}{d\theta} + V_z \frac{dp_{cyl}}{d\theta} \quad (2.16)$$

Where H_z is the enthalpy of the zone, $Q_{w,z}$ is the heat exchanged through the zone's walls, V_z is the zone's volume;

- Burning zone: the temperature is computed using the energy balance applied to the entire volume of burned gases and the zone which is sub-divided, knowing the mean temperature of the burned gases:

$$m_b h_b T_b = \sum_{i=1}^{Nz} m_i h_i T_i \quad (2.17)$$

Then, the heat exchange surface is derived by the control volume V_z using the assumption that each zone is spherical and centered in the spark plug.

2.2.2 Predicting combustion models

There are more possible models to be used in order to predict the combustion functioning, whereas two are the main important.

- Wiebe function, which is more simpler and based on a zero-dimensional approach, assuming that the cylinder content has a uniform composition and state at any time, so without any modeling of physical and chemical sub-process as fluid motion, injection, ignition or flame propagation.

The rate of energy release is so represented using quite simple mathematical relations, in order to reproduce the energy release observed by experiments.

The Wiebe function represents the burned mass fraction x_b using an S-shape curve that is function of the crank angle, defined as follows:

$$x_b = 1 - \exp \left[-a \left(\frac{\theta - \theta_i}{\theta_e - \theta_i} \right)^{m+1} \right] \quad (2.18)$$

Where: θ_i is the actual beginning of combustion, setted a few degrees after the spark timing, θ_e is the practical end.

The two parameters a, m are dependent from the geometry of the combustion chamber, and the first is called "efficiency factor" and measures the

completeness of the process (for example, for $a=6.9$ there's an $x_b(\theta_c)=0.999$, and for an $a=4.6$ there's an $x_b(\theta_c)=0.99$); whereas the second is the “shape factor” and measures the velocity of the process in its initial phase, such that the lower m is, the higher will be the initial energy release: this parameter is the one that can be reduced taking in account the effect of phenomenas like the exhaust gases recirculation, assuming generally values between 2 and 5.

The variation of the two parameters can bring to obtain a curve that can agree with the experimental datas derived from the pressure measured, as shown in figure 2.4:

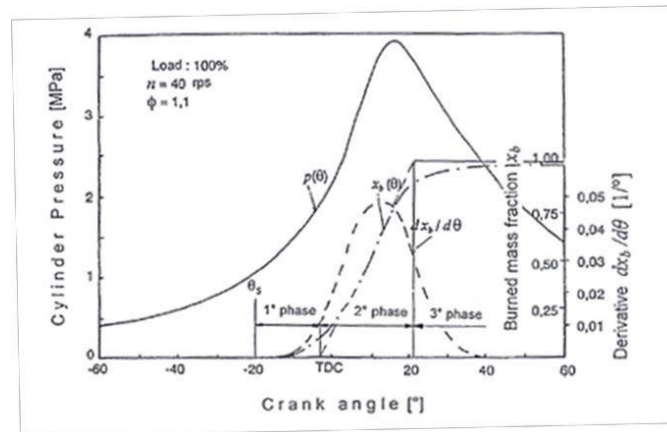


Figure 2. 4: Cylinder pressure and burned mass fraction represented using a Wiebe curve

- Advanced model: if it is necessary to have more complete and accurate results, there's the need to switch to a more precise model, which is the advanced one, characterized by a quasi-dimensional approach.

This model takes in account geometrical features as fluid motions and flame front propagation, which are added to the thermodynamic equations.

The quasi-dimensional approach is in between 0-D and 1-D, uses phenomenological equations that based on assumptions and relations derived from empirical observations, rather than pure theory.

Once the characteristics of the turbulent field are known there are many models that can predict the evolution of the turbulent flame front, using the assumption of Damkoler that the structure of the turbulent flame can be considered as derived by a lamnar reacting sheet, which border is wrinkled by turbulent fluid motion.

So, a turbulent combustion velocity w_{tc} can be defined as function of the laminar one w_{lc} (measured by the characteristic chemical reaction velocities) and a main parameter that takes in account the turbulent levels of reacting gases.

In GasDyn it is employed the Zimont combustion model, which is simple, robust and able to predict many experimentally observed phenomena using a low number of assumption and constrains, with only two main ideas:

1. in a spark ignition engine, since the fuel is fully vaporized and premixed with air and residual gases, the chemical reactions during the combustion process are slower than the turbulent motions, so the process is turbulence-controlled;
2. the effects of the different scaled turbulences must be treated separately, because the large eddies distort the flame front, and the small eddies (which have a scale that is smaller than the flame thickness) intensify the energy and mass transfer in the reacting zone.

The number of Damkohler is here used as a measure of turbulence influence on chemical processes, as a ratio between characteristic fluid turnover time in large eddies and characteristic reaction time:

$$Da = \frac{\tau_t}{\tau_l} = \frac{l_l t_{lf}}{u' w_{lc}} \quad (2.19)$$

Zimont, using dimensional analysis indications, proposed the following equations for the turbulent combustion velocity:

$$w_{tc} = c_z u' Da^{\frac{1}{4}} = c_z u' \left[\left(\frac{l_l / u'}{t_{lf} / w_{lc}} \right)^{1/4} \right] \quad (2.20)$$

$$w_{tc} = c_z u'^{3/4} l_l^{1/4} w_{lc}^{1/2} x_m^{-1/4} \quad (2.21)$$

Where c_z is an adjustable constant determined from experimental data and the laminar front thickness is assumed as proportional to the ratio between thermal diffusivity of the unburned mixture and the laminar combustion velocity:

$$t_{lf} = \frac{x_m}{w_{lc}} \quad (2.22)$$

2.3 Predicting emissions model

Since the main goal of this work is to investigate the effects on the emissions of the exhaust gas recirculation, the GasDyn code has the capacity of predicting the combustion products and give them in output expressed in part per million (PPM) concentration.

The computation of the combustion produced species is made under the assumption that, apart from NO and CO, all the other species are in thermodynamic equilibrium with respect to the burnt gas temperature of each zone.

Only the CO and NO, that are the most relevant species, are computed combining the thermodynamic equilibrium and the kinetic behaviour, imposing the conservation of the elements involved into the reactions.

In order to provide a better capability of the sub-chemical models and a better description of the pollutant formation process, the temperature stratification into the combustion chamber is taken in account by the model.

2.3.1 Carbon monoxide (CO)

The CO has a rapid formation, whereas its oxydation into CO₂ is slower, depending on temperature and cooling rate, so the process is modelled as follows:

1. CO formation within the flame front;
2. CO destruction within the burnt gases.

The formation of the CO happens into the flame front, assuming its concentration in equilibrium, then it is converted into CO₂ according to the rates in the following table:

Reaction	Reaction Rate [mol/ (cm ³ s)]	
CO + OH \rightleftharpoons CO ₂ + H	6.76 · 10 ¹⁰	· exp (T /1102)
CO + O ₂ \rightleftharpoons CO ₂ + O	2.50 · 10 ¹²	· exp (-24055/T)

Table 2.1: Reaction rates for CO formation/destruction

2.3.2 Nitric oxides (NO)

There are three kind of nitrous oxides that can be formed into a combustion processes:

1. Fuel NO_x: generated by atomic nitrogen present in the fuel that directly reacts with the oxygen;
2. Prompt NO_x: generated by a reaction between N₂ present in air and radicals into the flame front;
3. Thermal NO_x: directly generated by the oxydation of N₂ at high temperatures;

It has been observed that the most important phenomena that brings to the generation of NO_x is the third one, due to the really high temperatures that can be reached during the combustion process, expecially in the flame front zone, whereas the other two mechanisms do not have a significant importance, despite of some very rare conditions like really lean combustion or low temperatures.

After the combustion process it has been observed that most present of the NO_x species is nitrogen monoxide NO, that represents up to 98% of all the nitrogen oxides.

The reactions considered by the model and their rate is resumed in the following table, and are computed at the zone temperature T_z.

Reaction	A	b	Ta
(1) N + NO ⇌ N ₂ + O	0.33 · 10 ¹³	0.2	0.0
(2) N + O ₂ ⇌ NO + O	0.64 · 10 ¹⁰	1.0	3160
(3) N + OH ⇌ NO + H	0.38 · 10 ¹⁴	0.0	0.0
(3) N ₂ O + O ⇌ 2NO	0.69 · 10 ¹⁴	0.0	13400
(4) N ₂ O + O ⇌ N ₂ + O ₂	0.10 · 10 ¹⁵	0.0	14100
(5) N ₂ O + H ⇌ N ₂ + OH	0.7587 · 10 ¹⁴	0.0	7600

Table 2.2: Reaction rates for NO super-extended mechanism

Since the model has to use the concentration of many other species, that values have to be estimated: this happens using the chemical equilibrium model.

In order to improve the predictivity in a wide range of operating conditions as needed in this case, due to the presence of EGR and the partial load, the mechanism adpted is the Zeldovich super-extended, that involves 67 reactions and 2 different species.

In this model the only specie wich concentration is computed kinetically is NO, whose values are integrated step-by-step by a Runge-Kutta method that calculates the other thermodynamic proprieties.

In order to obtain the convrgence of the integration process, a variable-step method is needed.

2.3.3 Unburned hydrocarbon (HC)

The unburned hydrocarbons are generally due to an incomlete combustion, but there are many phenomena that can bring to that, and a complete description of the formation process that can be robust and reliable nowadays is not available.

In GasDyn there are taken in account, for a spark ignition engine, the following mechanisms:

1. Crevice effect, so the fact that the mixture into the volume between the piston ring and the cylinder wall represented in figure 2.4 cannot be reached by the flame, that quenches at the entrance.

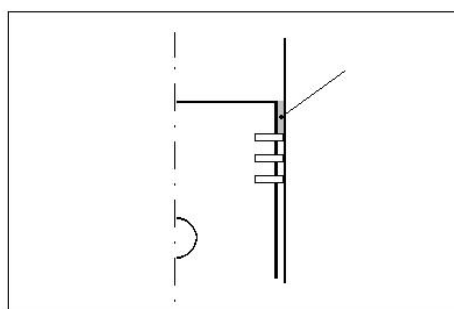


Figure 2. 5: crevice volume

Due to the high surface/volume ratio of the crevice, the mixture trapped, which is at the same pressure of the chamber, is rapidly cooled at the piston temperature and so is more difficult to burn.

It is evident that there's a geometrical basis on the quantity of fresh mixture trapped into this volume, and taking in account that fact is possible to account for a complete cycle the hydrocarbon storage and release of the crevice volume.

2. Adsorption of fresh mixture into the oil layer on the cylinder walls: according to Henry's law, the adsorption occurs during the intake phase until the saturation of the layer, and the desorption happens during the exhaust one.

Assuming that the oil film is at the same temperature of the walls, the fuel is constituted by a single hydrocarbon specie and representing the oil as $C_{30}H_{62}$, it is possible to compute the mass concentration of fuel adsorbed by the oil:

$$\frac{\partial Y}{\partial t} - D \frac{\partial^2 Y}{\partial x^2} = 0 \quad (2.23)$$

Where Y is the mass fraction of fuel, t is the time, x is the distance from the wall and D is a relative diffusion coefficient, which depends by the temperature, the oil viscosity and the molar volume of the fuel at normal boiling conditions.

3. Partial burn effects due to quench layer, which cannot be physically described in a quasi-dimensional approach but represented by a semi-empirical correlation proposed by Lavoie:

$$F_{prb} = C_1 \exp\{-(\theta_{evo} - \theta_{90})/[C_2(\theta_{90} - \theta_0)]\} \quad (2.24)$$

Where F_{prb} is the unburnt charge remaining in the cylinder, C_1 , C_2 are experimental-based parameters.

4. In-cylinder oxydation: all hydrocarbons released into burned gases undergo a complex mechanism of oxydation due to the presence of high temperature in the chamber.

In this sense, GasDyn uses a simplified approach to account for this process, using an Arrhenius equation:

$$\frac{d[HC]}{dt} = -C_r A e^{E/(RT^9)} [HC][O_2] \quad (2.25)$$

In this equation Cr is a calibration factor, usually equal to 0.2, A is a pre-exponential factor, e the activation energy of the reaction, R the molar gas constant.

5. Soot, which is the particulate, estimated using the Hiroyasu mass equation:

$$\frac{dm_s}{dt} = \frac{dm_{sf}}{dt} - \frac{dm_{s,ox}}{dt} \quad (2.26)$$

Where the mass of soot increase rate is equal to the difference between soot mass formation and soot mass oxidation.

This rates are computed as follows:

$$\frac{dm_{sf}}{dt} = A_f m_{fv} p^{0.5} \exp\left[\frac{E_{sf}}{RT}\right] \quad (2.27)$$

Where m_{fv} is the mass of fuel vaporized and the activation energy is setted at 52335 kJ/kmol;

$$\frac{dm_{sf}}{dt} = \frac{6MW_c}{\rho_s D_s} R_{tot} m_s \quad (2.27)$$

Where MW_c is the carbon molecular weight, ρ_s is the soot density, D_s is the characteristic soot particle diameter and R_{tot} denotes the total soot oxidation, equal to:

$$R_{tot} = \left(\frac{k_A p_{O_2}}{1 + k_z p_{O_2}}\right) x + k_B p_{O_2} (1 - x) \quad (2.28)$$

Where x is the fraction of the more reactive site on the carbon surface and k_A , k_B , and k_z are the Arrhenius rate constants whose value is taken usually from literature.

CHAPTER 3: TURBOCHARGED ENGINE AND GASDYN MODELING

3.1 The turbocharged engine

One of the main issues with a naturally aspirated engine is that the same engine has to spent work in order to bring the fresh charge into thy cylinders, facing al the losses due to pipe friction and local pressure drop sas valves and curves.

This brings to a limit at the maximum quantity of fresh charge that is possible to pump into the chamber: the real mass of air trapped in the cylinder is less than the theoretical one, wich is the mass of air occupying the cylinder's volume at atmospheric pressure.

In this sense, the “volumetric efficiency” of the naturally aspirated engine is lower than one, even adopting straight and large pipes and increasing the valves' diameter.

Starting from the '20s of the XX century, when the first examples of motorsport were born, the need of increasing the volumetric efficiency of the internal combustion engine was really high, and so the first ideas of using a compressor to drive the charge into the cylinders were made.

Initially, the use of a mechanical compressor driven by the engine was the most used layout, even for aircraft engines, due to the fact that it helped reducing the power loss given by the reduction of air density at high altitude.

This kind of forced induction is now called “supercharging”, and the first real turbocharger has been patented in 1905 by the swiss engineer Alfred Bucchi, wich

thought to use an exhaust-gas turbine to drive the compressor, applying it on a Sulzer marine engine, like the one in figure 3.1.

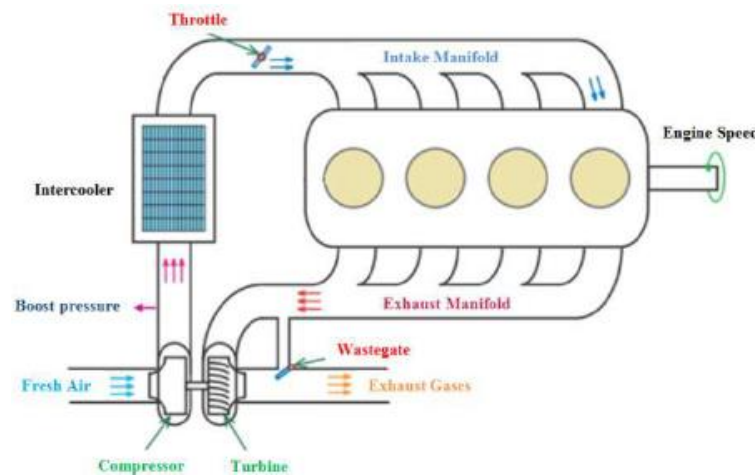


Figure 3. 1: Turbocharged 4-cylinder engine, with intercooler and waste-gate valve.
Notice that the turbine and the compressor have a common shaft, which has to bring the mechanical power from the turbine to the compressor.

This kind of supercharging, despite being more difficult to realize, had the main advantage of using the residual enthalpy of the exhaust gases for driving the compressor, without stealing power to the engine crankshaft.

Other positive effects of the turbocharging are that this system is very overload capable and can regulate itself.

Since generally the machines do not have to elaborate a high massflow, so their dimensions must be reduced even for finding them a place into the engine, the most used solution is to adopt a radial centrifugal/centripetal structure.

Due to the pressure waves into the ducts generated by the unsteady functioning of the engine, there have been implemented two different schemes of turbocharging: constant pressure one and impulse one.

In the first case, the pressure waves are dissipated into a plenum setted after the exhaust manifolds, so the turbine faces a more regular expansion ratio and more steady functioning, which allows to a longer duration.

This solution has the drawback of being dissipative, since the wave energy is not exploited, so nowadays the most used solution is the impulse turbocharging, where the exhaust manifolds are designed in order to provide to the turbine the maximum energy with the lowest unsteadyness possible, studying the engine phasing.

Starting from the '80s the turbocharging has become more and more used on automotive engine, and now the whole diesel engines and a huge part of gasoline ones use that solution, because allows to increase performance without increasing too much the fuel consumption, or keeping constant the performances reducing the engine's displacement, wich is called "downsizing".

The engine studied in this work canbe assumed as a god example of downsizing, because can provide a very high torque with respect to its relatively low displacement.

3.1.1: Turbocharger implementation in Gasdyn

GasDyn can run a simulation of a turbocharged engine, and into the code the compressor and the turbine are modeled using performance maps that are uploaded by the user.

These maps are summarized into a series of working points described by rotational speed, pressure ratio, massflow rate and thermodynamic efficiency.

When the working point is near the stall, or due to the fact that the speed lines can be flat, the code has an algorithm that reduces the magnitude of any excessive fluctuation, expecially in the compressor.

For this one, the working points are fitted by polynomial curves, assumming for each rotational speed that the first experimental point is the limit or the choaked flow, as shown in figure 3.2:

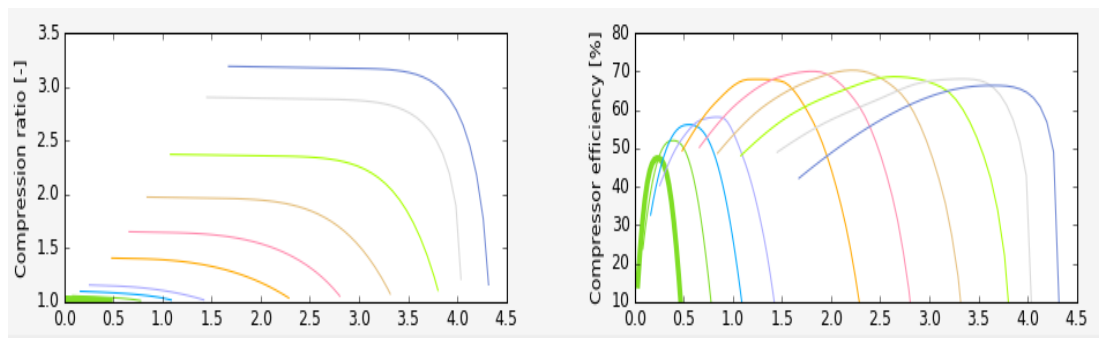


Figure 3. 2: Example of interpolated curves for a compressor.

For a turbine, the maps are made by points that correlate the expansion ratio, the reduced massflow, the thermodynamic efficiency and the turbocharger shaft speed. Since usually the manufacturers provide these maps only for points near the maximum efficiency, but during the functioning the turbine could go far from these working points, an extrapolation of a wider map is necessary.

For a good dataset, the procedure is the following:

- The optimal blade speed ratio (BSR) calculated at the maximum efficiency point for each speed line, should increase linearly with the expansion ratio;
- The operative points at maximum efficiency increase linearly with respect to the expansion ratio, too;
- The ratio between massflow at maximum efficiency and the highest massflow should be linear with the rotational speed when this last is low, and then a smooth monotone positive curve with one local maximum.

So, defining the BSR as:

$$BSR = \frac{u}{c_{is}} \quad (3.1)$$

Where c_{is} is the speed of sound, defined:

$$c_{is} = \sqrt{2C_p T_{01} (1 - \beta^{(1-\gamma)/\gamma})} \quad (3.2)$$

And the rotor tip speed u is computed as:

$$u = \frac{2\pi RPM D}{60 \cdot 2} \quad (3.3)$$

Then, maximum efficiency points are fitted by a linear regression and extrapolated over a wider range of expansion ratios.

Also, the normalized massflow ratio:

$$m'_{norm} = \frac{m'}{m'_{opt} RPM_i} \quad (3.4)$$

Is plotted against the pressure ratio at the maximum, and fitting curves are used for extracting values for the computation of normalized quantities, in order to achieve non-dimensional plots.

For each experimental expansion ratio, the normalized quantities are computed as follows:

$$m'^* = \frac{m'_{exp}}{m'_{opt}} \quad (3.5)$$

$$BSR^* = \frac{BSR_{exp}}{BSR_{opt}} \quad (3.6)$$

The final result of the extrapolation is resumed then in figure 3.3 with the turbine curves represented in GasDyn pre-processor:

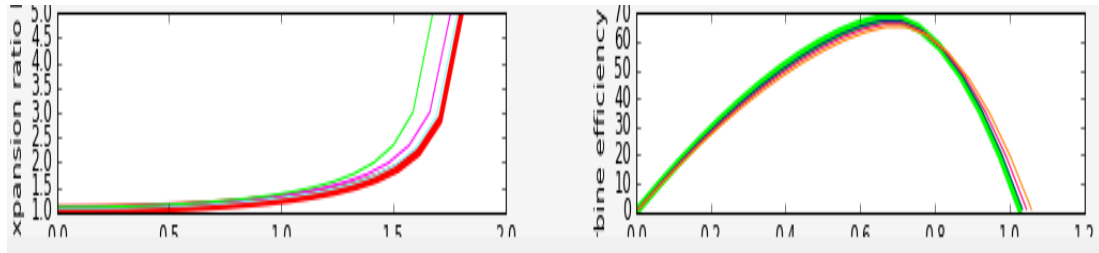


Figure 3. 3: Turbine curves after data extrapolation.

Once the maps are ready, the code has to compute the balance between the compressor and the turbine, based on a torque balance on the shaft:

$$T_T - T_C - T_{loss} = I\alpha \quad (3.7)$$

Where T_T is the torque developed by the turbine, T_C the torque absorbed by the compressor, T_{loss} the transmission loss due to mechanical friction, I is the polar momentum of inertia of the rotating part (usually computed by simulations) and α is the instantaneous angular acceleration.

The torque values are written in the following way:

$$T_T = \frac{W'_T}{2\pi N_T} \quad (3.8)$$

$$T_C = \frac{W'_C}{2\pi N_T} \quad (3.9)$$

$$T_G = \frac{W'_G}{2\pi N_T} \quad (3.10)$$

Where W'_T , W'_C , W'_G are the power developed by the turbine and absorbed by the compressor and the mechanical bearings.

By substituting the torque expressions in the balance of equation 3.7, it is found that:

$$\frac{dN_T}{dt} = \frac{1}{2\pi I} (\eta_M T_T - T_C) \quad (3.11)$$

Where η_M is the mechanical efficiency of the turbocharger, computed as:

$$\eta_M = \frac{W'_T - W'_E}{W'_T} \quad (3.12)$$

The first term of the balance 3.11 expresses the fluctuation in turbocharger speed, and it is acceptable when under the value $\varepsilon=0.5\%$.

CHAPTER 4: EMISSIONS AND EGR SYSTEM

4.1: Pollutant emissions

As it is widely known, an internal combustion engine contains in the exhaust gases many pollutant species, and this is recognized as a very big issue, especially in urban areas where the concentration of pollutant sources is higher.

The combustion process, depending on its quality, produces mainly the following species, which have different noxious effects on human and environmental wealth:

Specie	Impact
Carbon monoxide (CO)	Poisoning, cardiovascular diseases
Unburned hydrocarbons (HC)	Phototermica smog
Particulate matter (PM)	Lung damages
Nitrogen oxides (NO _x)	Acid rains, toxic chemicals
Sulphur oxides (SO _x)	Smog, acid rains, lung diseases
Carbon dioxide	Global warming responsible

Table 4.1: Emitted species and their noxious effects

Starting on the 70's, the interest of the human effect on the environmental quality has risen, so the first legislation on the emissions took place.

Nowadays, for European automotive market, the normatives about emissions are the “Euro” standards, which are distinguished by a number (Arabic for cars, Roman for industrial vehicles) depending from the year of introduction.

The first introduction of this legislation was in 1992, then the vehicles produced before are now considered “Euro 0”.

The last of these is the “Euro 6”, established in 2011, which has been updated with many classes characterized using a letter, reaching “Euro 6d” starting from 2019 in a temporary way and definitively in 2021.

These normatives are based on measurement made on the exhausts of the vehicles while subjected to an homologation test that simulates real driving conditions, whereas the reliability of these test is still under discussion.

Actually the used one is the NEDC (New European Driving Cycle), which duration is 1180 seconds, articulated as shown in figure 4.1:

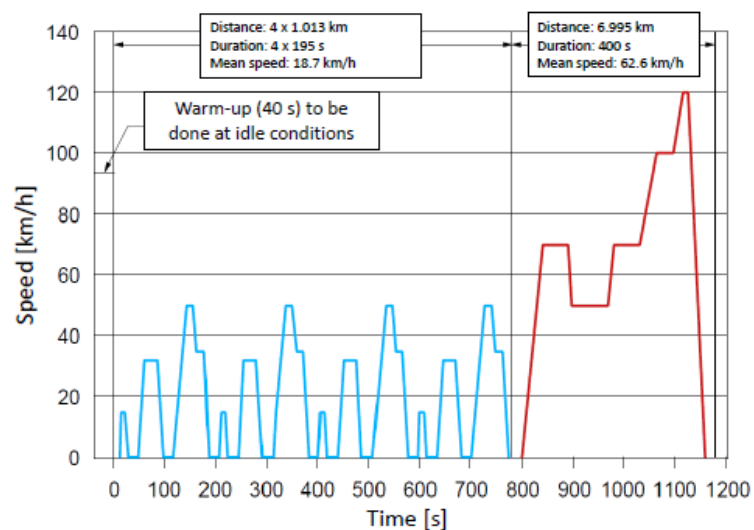


Figure 4. 1: Composition of the NEDC homologation test.

This test has been criticized due to the fact that it is too distant from real driving conditions, which are more engaging for the engine, so the emissions registered could be lower than real-use ones.

There are many solutions under study, the most important is the new WLTC (World Light duty vehicle Test Cycle), characterized by a higher duration and a class subdivision depending from the PMR, so the ratio between engine power and kerb weight.

An example of WLTC cycle is shown in figure 4.2:

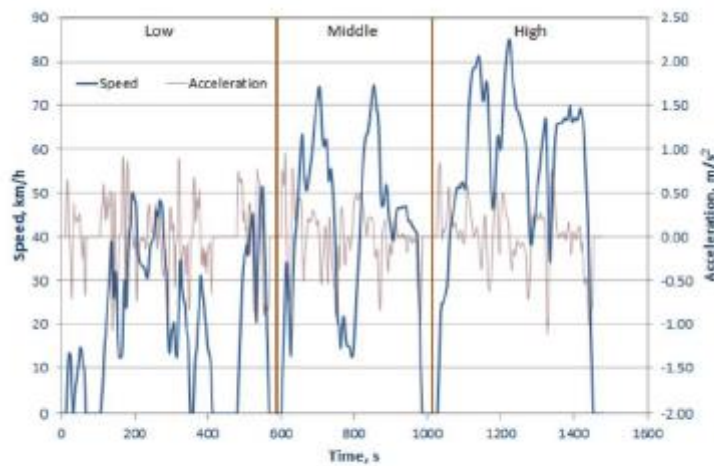


Figure 2. WLTP Cycle for Class 2 Vehicles

Figure 4. 2: WLTC cycle for Class 2 vehicles, with a PMR between 22 and 34.

Another possible strategy under studies is the possibility of using portable emissions measurement systems (PEMs), but is yes from being realized.

Unless the actual strategies has achieved a good emission reduction, the need of limiting that issue is still important, and this brings to a continuative decrease of the maximum amount of pollutant species.

Even if it has always been considered a problem related to the diesel engines, the last Euro normatives has imposed a huge reduction on NOx and particulate matter, wich is difficult to achieve with only the 3-ways cathalitic converter.

Step	Date	CO	HC	HC+NO _x	NO _x	PM
SI engine						
Euro 1	1992/07	2.72	--	0.97	--	--
Euro 2	1996/01	2.20	--	0.50	--	--
Euro 3	2000/01	2.30	0.20	--	0.15	--
Euro 4	2005/01	1.00	0.10	--	0.08	--
Euro 5	2008/09	1.00	0.10	--	0.06	0.005
Euro 6	2014/09	1.00	0.10	--	0.06	0.005

*All emissions in g/km

Figure 4. 3: Euro emission limits for spark ignition engines.

If for the PM is being implemented the gasoline particulare filter, for the nitrogen oxydes the use of an EGR system is representing a good way to follow.

4.2: EGR system.

As introduced in the chapter before, the NO_x formation mechanism for an internal combustion engine used in automotive is mainly due to the high temperatures reached during the combustion.

There are many parameters that can affect the maximum temperatures, such as:

- Air/fuel ratio of the mixture;
- Spark advance;
- Speed and load.

Unfortunately, there are technical limits on the values of these parameters: as an example, a lean air/fuel ratio could help the reduction (figure 4.4), but this avoids a good functioning of the 3-ways catalyist that needs a stoichiometric mixture.

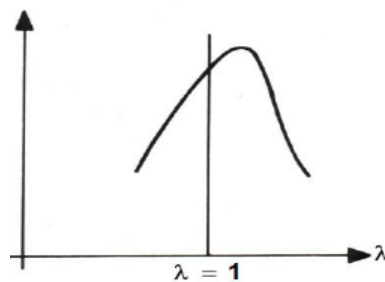


Figure 4. 4: effect of the air/fuel ratio on the NO_x production.

A good solution for reducing the combustion temperature is to introduce an inert into the combustion chamber, in a way to absorb part of the heat produced.

This inert is easily find using the exhaust gases, that can be partially recirculated into the system as shown in figure 4.5:

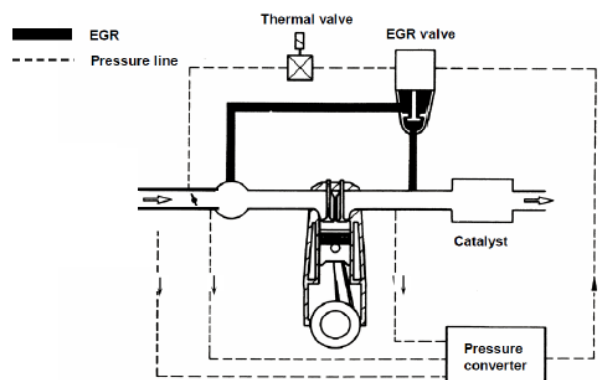


Figure 4. 5: Example of an EGR (exhaust gas recirculation) system.

Depending from the percentage of recirculation, which is regulated by an apposite valve, there will be more or less inert added in the mixture, which will bring to a certain temperature reduction and so to a lower production of nitrous oxides.

For the particular case of a turbocharged engine, there are two possible strategies of implementation of the EGR, depending from the path of the exhaust gases:

- Short route/High pressure, if the gases are prelevated before the turbine on the exhaust manifolds: this means that the injection will happen downways with respect to the compressor, so the gases are at “high pressure”.

This solution seems being the simpler one, but it is evident that the exhaust gases are taken at a high temperature, so even by cooling them they will still be hot, and the final temperature reduction won't be too high.

- Long route/Low pressure, when the gases are prelevated after the turbine, so expanded, and injected before the compressor, at a pressure which is not too higher with respect to the atmospheric one.

This scheme has the drawback of using generally longer ducts, but provides a better temperature reduction because adds colder gases.

It is important to remember that, since the recirculation provides a lower maximum temperature and so a slower combustion, and the presence of an inert occupies a space in the chamber that cannot be exploited for fitting fresh charge, this strategy of reduction is used only at partial load, whereas at full load there's no recirculation in order to extract the maximum performances from the engine.

CHAPTER 5: ENGINE VALIDATION AND SIMULATIONS

5.1: Engine validation.

The engine adopted for this work is the Alfa Romeo 1.8 TBi, a gasoline turbocharged engine which can be assumed as a good example of downsizing, since it can provide a very good torque curve and maximum power despite the relatively low displacement. It shows many advanced solutions for improving the performances, as continuous-variable valve timing on both sides and a valve crossing at low/mid regimes that allow for a better scavenging, possible due to the presence of a direct injection system.



Figure 5. 1: Alfa Romeo 1.8 TBi engine

This engine has been used without the EGR system on many Alfa Romeo models, and was produced in two different version, one with a cast iron basement wich provided 147 kW, and another with aluminuim basemend wich was rated for 172 kW, that represents the choiche for this work.

The main characteristics are resumed in the following table:

Engine type:	Otto cycle, gasoline turbo
Cylinders:	4, inline
Bore [mm]	83
Stroke [mm]	80,5
Valve number	16
Displacement [cmc]	1742
Compression ratio	9,8:1
Intake valve diameter [mm]	30
Exhaust valve diameter [mm]	27
Firing order	1-3-4-2
Injection system	GDI

Table 5. 1: Characteristics of the 1.8 TBi engine.

The first passage has been modeling the enigne in its stock configuration on GasDyn, as shown in figure 5.2, in order to check the reliability of the previsions made by the simulations.

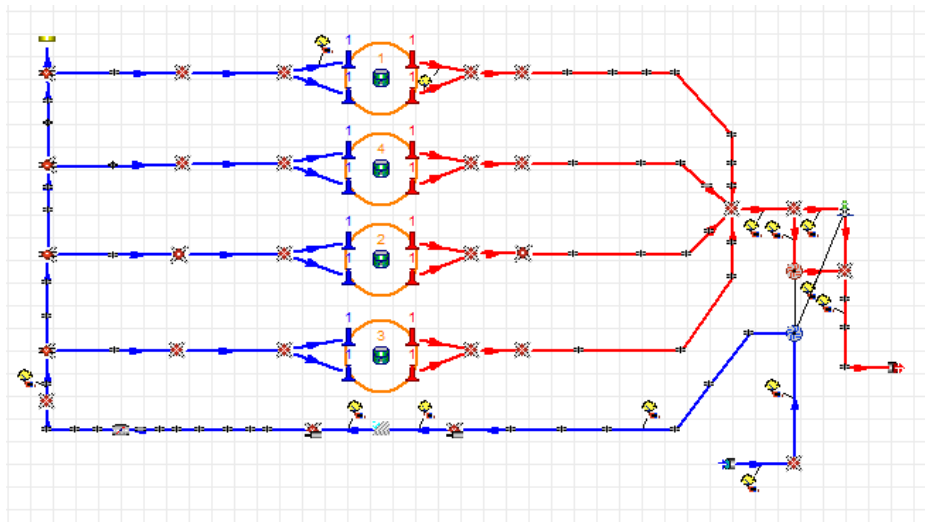


Figure 5. 2: Engine model into the GasDyn editor.

Then a full load simulation has been realized, and the values has been available for the comparison with the experimentally collected ones.

As shown in figure 5.3, the performances computed are nearly comparable to the real ones, so this means that the model is reasonably reliable.

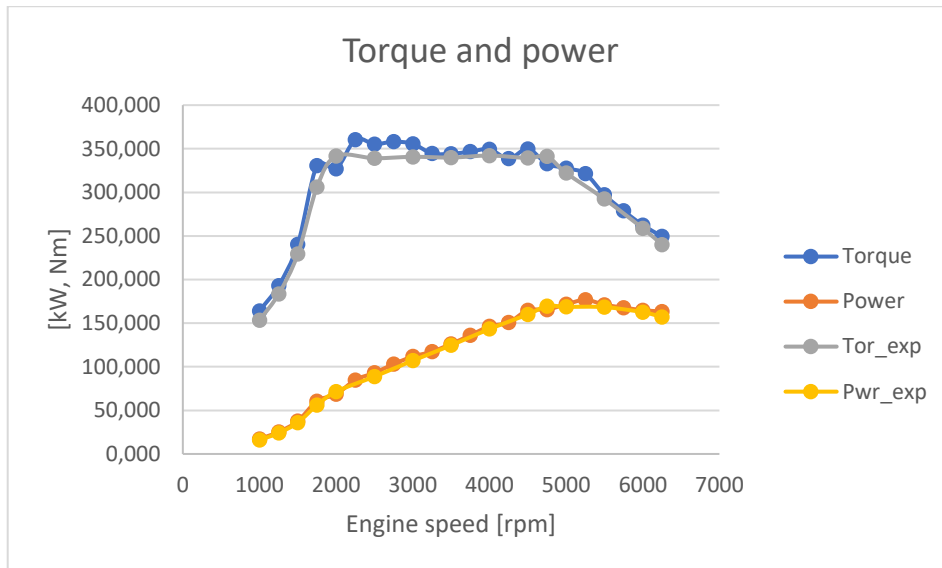


Figure 5. 3: Comparison between experimental and computer performances of the engine: the higher ones are the torque curves, and the lower ones the power curves.

An important thing to consider, working on a turbocharged engine, is the convergence of the process shown in chapter 3.1.1 that computes the turbocharger equilibrium.

In figure 5.4 is possible to see that, thanks to the GasDyn output, the sequence of values computed for the turbine and compressor power values compared and their discrepancy, until the convergence of the two values has been reached, as an example at 2000 rpm.

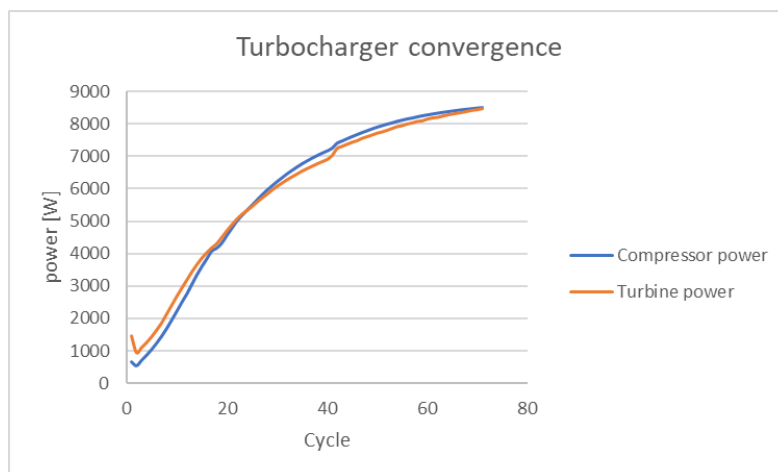


Figure 5. 4: Convergence of the compressore and turbine power.

The next step has been the realisation of a partial load model, assuming more or less the 50% of the maximum engine load, expressed as torque.

This is necessary due to the fact that the EGR system is applied only at partial load, since at the maximum power the most important thing is the performance, and the emissions are “secondary”.

Despite this, applying the EGR only at lower loads is still important because the highest number of possible working conditions of the engine are these, and so the pollutant emissions reduction becomes more important.

5.2: Part load and EGR models implementation.

5.2.1: Part load model.

The partial load model has been realized using the same layout, adopting the same combustion control system, which is an open-loop one with control on injected fuel mass and spark advance.

The fuel mass has been set at the half of the value in full load, and then the regulation of this parameter, the throttle and boost pressure has been made in order to reach a more or less stoichiometric combustion at the desired working point.

There are six working points selected, in order to try to cover more possible engine speed, whereas they're more concentrated in the medium/low regimes, the most used in the daily driving and the ones near the maximum torque, as shown in figure 5.5 and 5.6:

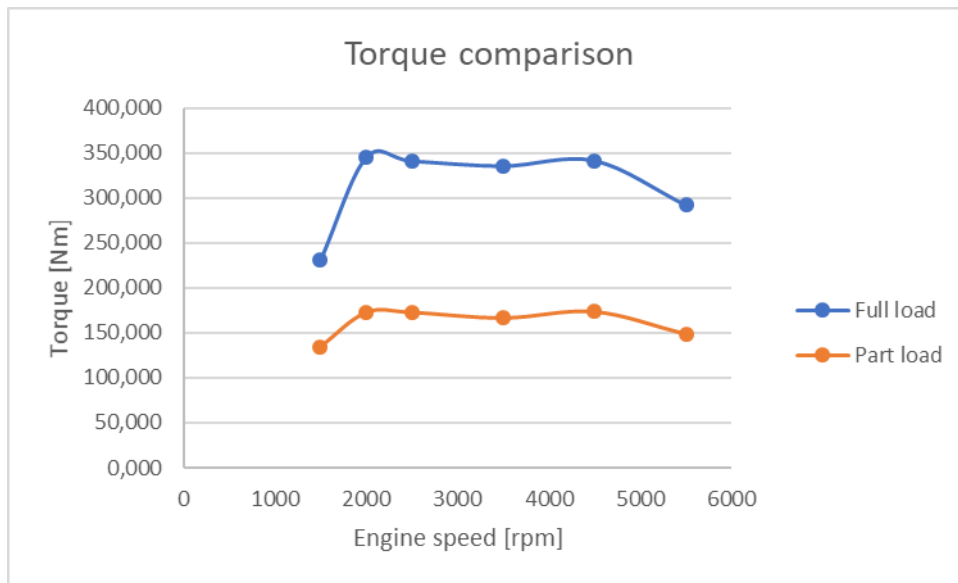


Figure 5. 5: Torque at part load compared with the full load curve

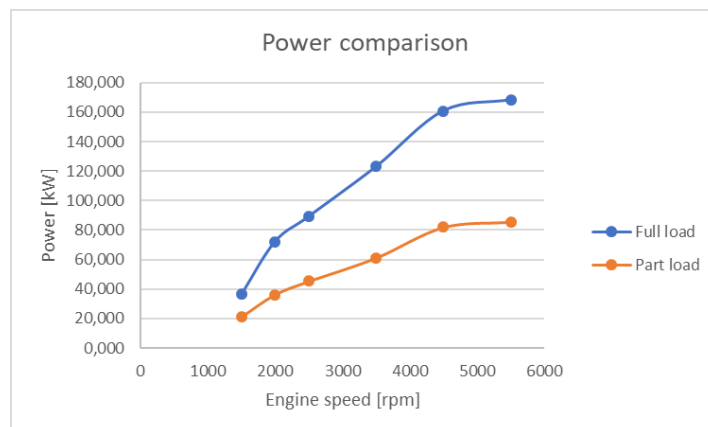


Figure 5. 6: Engine power at part load compared with the full load curve.

The values of boost pressure and throttle opening adopted are visible in figures 5.7 and 5.8, whereas in table 5.2 the injected fuel mass at every selected regime is shown.

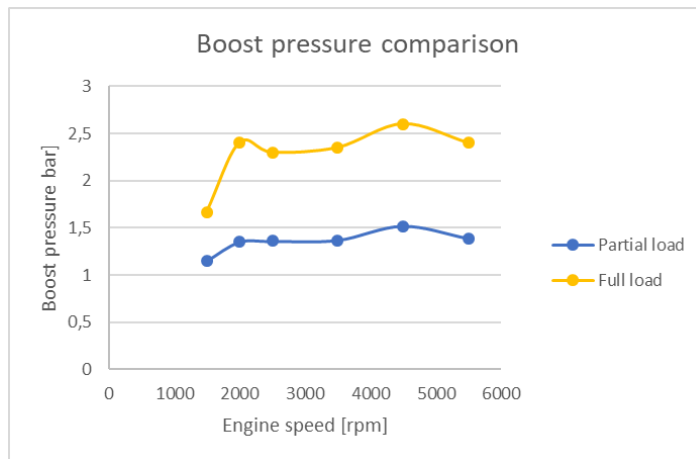


Figure 5. 7: Boost pressure at full load and part load.

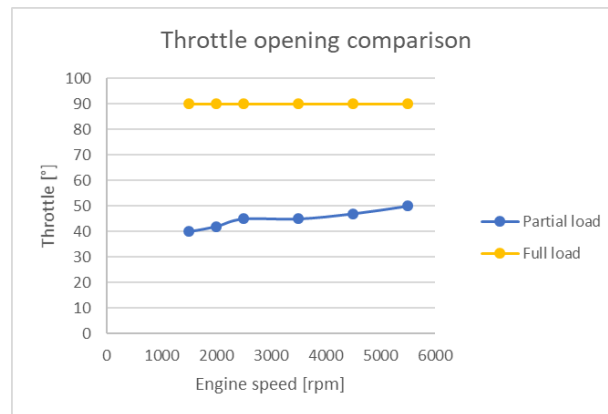


Figure 5. 8: Throttle opening at full load and part load

Regime [rpm]	Fuel mass [kg]	Spark advance [°]
1500	3,19E-05	-6
2000	4,31E-05	-1
2500	4,22E-05	-2
3500	4,19E-05	-6
4500	4,45E-05	-6
5500	4,02E-05	-11

Table 5. 2: Mass of fuel injected and spark advance for the investigated regimes

For the comparison that will happen with the EGR added layout, has been even computed the emissions of nitrous oxides at every regime (figure 5.9).

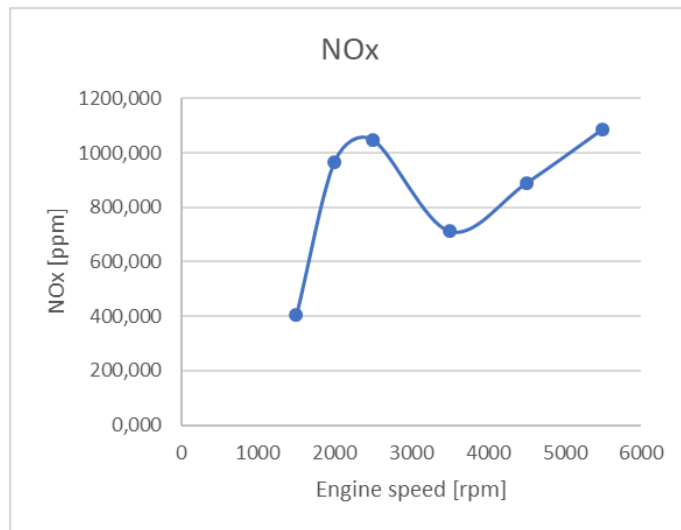


Figure 5. 9: NOx emissions without EGR.

5.2.2: Short route EGR system.

The first EGR system that has been implemented is the short route, which is the one that operates at high pressure.

Its layout, despite the GasDyn representation showed in figure 5.10, provides generally shorter pipes with respect to the low pressure strategy, whereas the temperatures are higher.

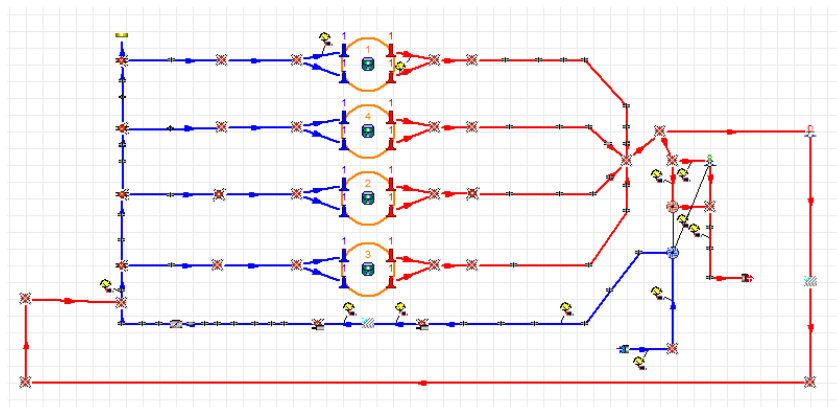


Figure 5. 10: GasDyn editor view of the short route EGR.

An important component of every EGR system is the cooler, which is a gas/water heat exchanger built using the shell-and-tubes configuration.

In this work it has been modeled using the “duct matrix” element, sized 20 centimeters long and 15 centimeters of diameter.

This kind of element allows two possible functioning strategies:

- With PID regulator, where the user can set the required temperature drop, here assumed equal to 50°C, and the system will provide it changing the heat exchange factors.
- With fixed wall temperature, which requires a lower computational effort but is not able to guarantee a certain cooling effect.

In order to reach the same working conditions (figure 5.11), it has been necessary to act on the throttle opening and on the boosting pressure of the compressor: since a part of the combustion chamber volume is occupied by the recirculated gases, for the maintenance of the stoichiometric conditions the same mass of air has to be delivered at a slightly higher pressure, and this necessity grows with respect to the engine speed.

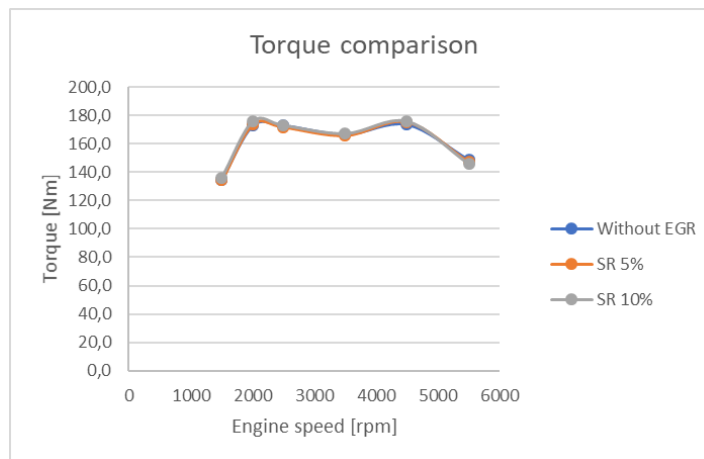


Figure 5. 11: Torque comparison between the three cases.

The solution so is adopting a coupling between throttling and boosting pressure that are globally higher than the standard values, as shown in figure 5.12 and 5.13.

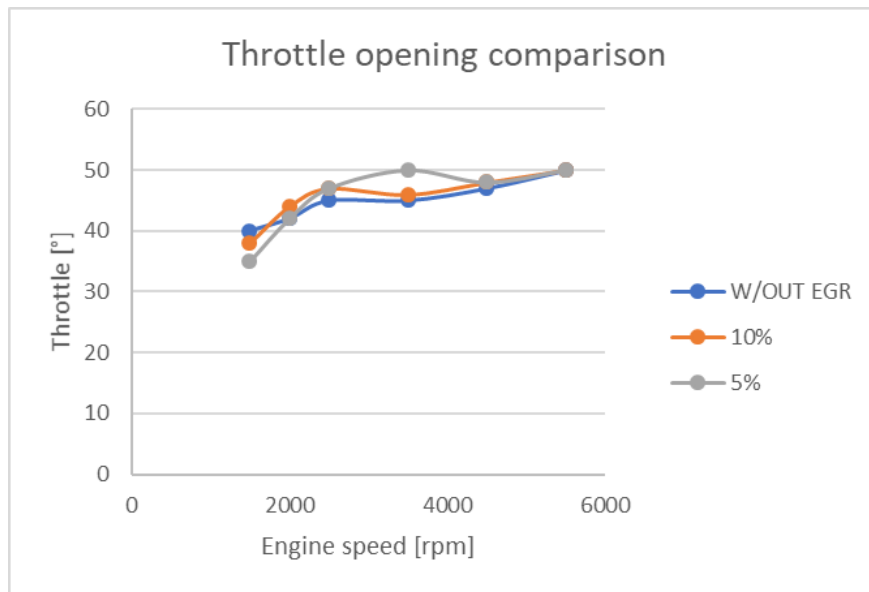


Figure 5. 12: throttle opening angles for the three different layout.

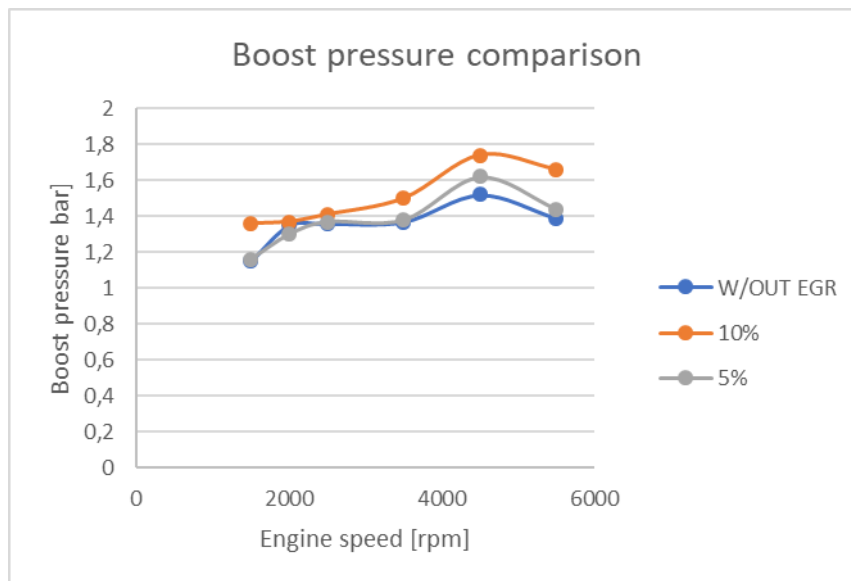


Figure 5. 13: target boost pressure for the three different layout.

Due to its positioning, the short route EGR is limited about the maximum recirculation achievable: as shown in table 5.3, the recirculation ratio, given as output by GasDyn into the “Purity” files, is not precisely reached and at 10% at lower regimes the differences become really important.

This is mainly due to the low pressure difference between intake and exhaust on this layout, and to many unsteady wave effects, that bring to a reduction on the recirculation at low/mid regimes and an increase at higher ones.

Regime [rpm]	EGR rate	Diff %	EGR rate	Diff %
	5%		10%	
1500	0,0521	4,20%	0,0965	-3,50%
2000	0,046	-8,00%	0,0749	-25,10%
2500	0,0476	-4,80%	0,0801	-19,90%
3500	0,05	0,00%	0,0952	-4,80%
4500	0,0496	-0,80%	0,0969	-3,10%
5500	0,0517	3,40%	0,097	-3,00%

Table 5. 3: Difference between real and target recirculation rate.

Anyway, the short route system has shown a good effectiveness, as is possible to see in figure 5.14.

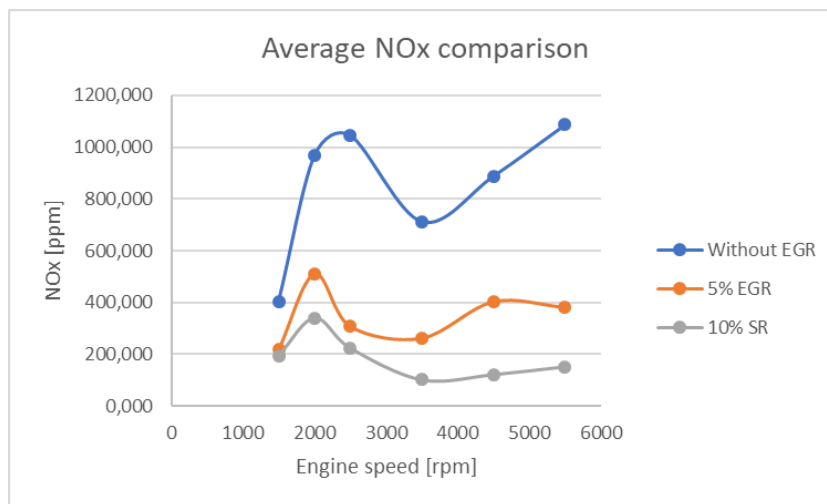


Figure 5. 14: Average NOx emissions on the four cylinders at different EGR rates.

It is evident that both the solutions bring to a good reduction of the NOx emissions, whereas the values reached using 10% of recirculation are not really reliable due to the difficult of achieving the real rate, so are possibly related to higher or lower values.

It is interesting to see that, despite at 2500 rpm the real recirculation rate is higher in the orange curve, its emissions are lower: this is due to the fact that, for reaching the

same working conditions, the boosting pressure for the 10% curve is higher, and so there's more air entering the cylinder bringing to a not-purely-stoichiometric combustion, which generates lower NOx.

The lower rate, despite all, shows a good emissions reduction (NOx are more or less a half with respect to the standard configuration) and is more reliable into a real application.

Looking at the in-cylinder temperatures, it is possible to see that actually there is a reduction on the peak values, which grows with respect to the EGR ratio.

Due to the fact that the recirculated gases are at a relatively high temperature, the reduction is limited under 100°C, and difference into the temperature reduction within the two different rates is not too much, as shown in figure 5.15 and 5.16.

It is even possible to see that another effect of the adding of an inert is the slowing of the process: the temperature slope in the recirculating cases is slower.

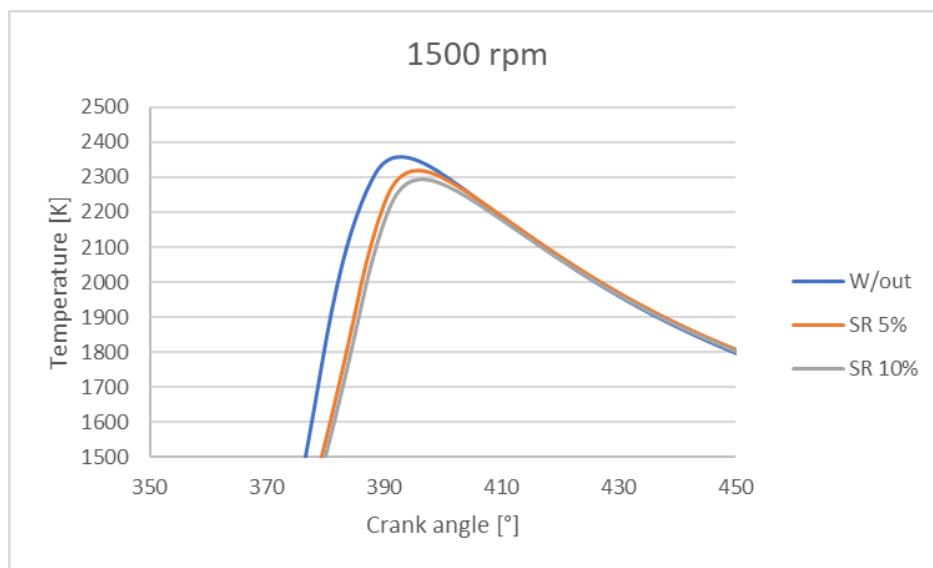


Figure 5. 15: in-cylinder temperatures at 1500 rpm at different recirculation rates

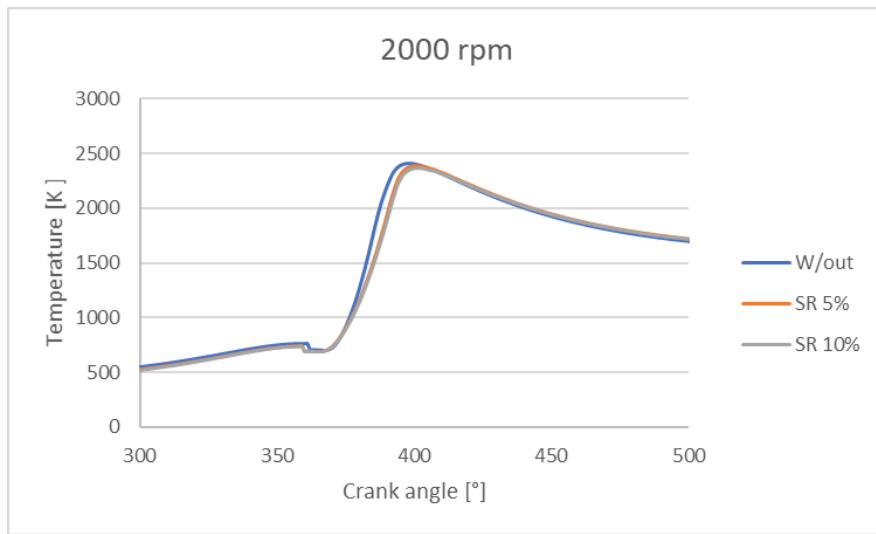


Figure 5. 16: in-cylinder temperatures at 2000 rpm at different recirculation rates.

The difference of effect becomes more important only when the real recirculation ratios are higher: in figure 5.17 is possible to notice that, with a real ratio equal to 11.8% instead of 10% the difference becomes more sensible and the reduction rises at more than 100°C.

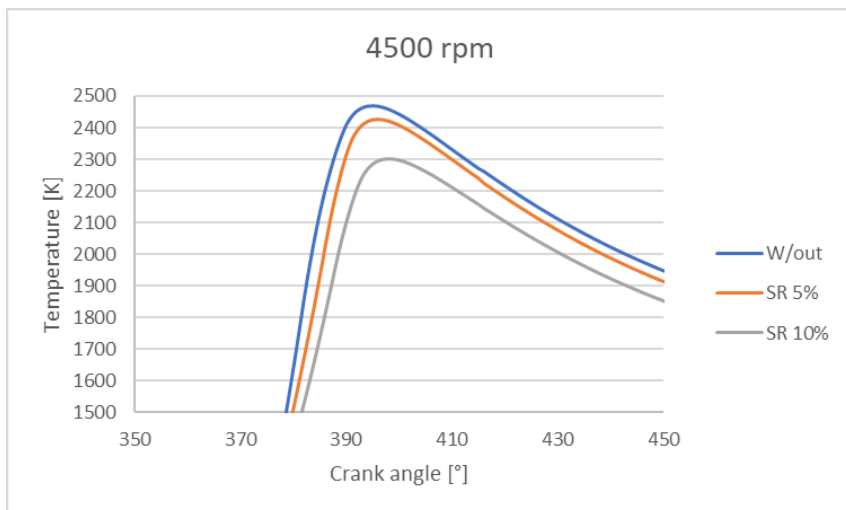


Figure 5. 17: in-cylinder temperatures at 4500 rpm at different recirculation rates.

Seems logic to say that the increase of the recirculation ratio, when possible, helps more at high regimes, whereas more difficult to exploit.

5.2.3: Long Route EGR system.

The second and more important system implemented is the long route, which operates at lower pressure.

The chosen layout is described in figure 5.18:

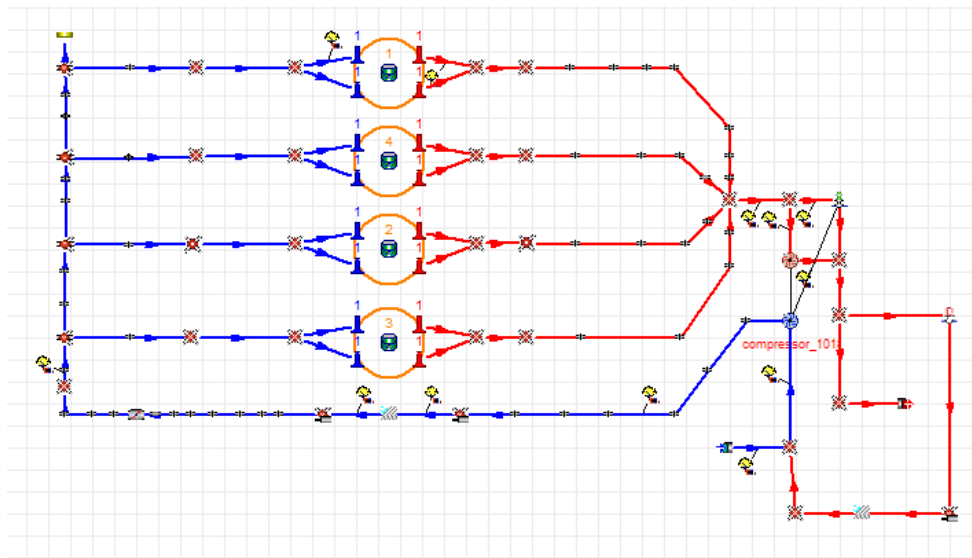


Figure 5. 18: Long route scheme on GasDyn editor.

There are two main advantages for the long route scheme:

- Since the exhaust gases are prelevated downstream the turbine, their temperature will be lower, and so the inert effect more sensible.
In this work it is important to notice that, due to the use of the PID regulation on the EGR cooler, its effect is the same on both short and long route.
- Since there are two machines between the EGR junctions and the cylinders, the unsteady and wave effects are reduced, and so is possible to control better the recirculation, achieving higher rates without excessive effort.

The different behaviour obviously affects the engine working parameters, since the boosting pressure and the throttling are different with respect both the standard and the short route, even considering the same recirculating ratio.

One evident thing is that the real exhaust gases added are nearer to the target ones, as possible to see in table 5.4.

Regime [rpm]	EGR rate	Diff %	EGR rate	Diff %
	SR		LR	
1500	0,0965	-3,50%	0,1085	8,50%
2000	0,0749	-25,10%	0,1353	35,30%
2500	0,0801	-19,90%	0,1275	27,50%
3500	0,0952	-4,80%	0,1029	2,90%
4500	0,0969	-3,10%	0,0997	-0,30%
5500	0,097	-3,00%	0,0998	-0,20%

Table 5. 4: Real recirculation ratios for short and long route.

This brings to a different boost/throttle couples for achieving the same working points, as shown in figure 5.19 and 5.20:

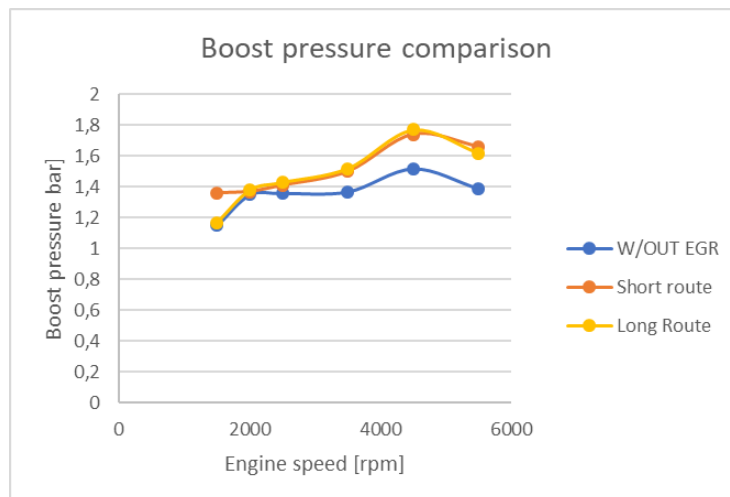


Figure 5. 19: Boost target pressure for the three main cases.

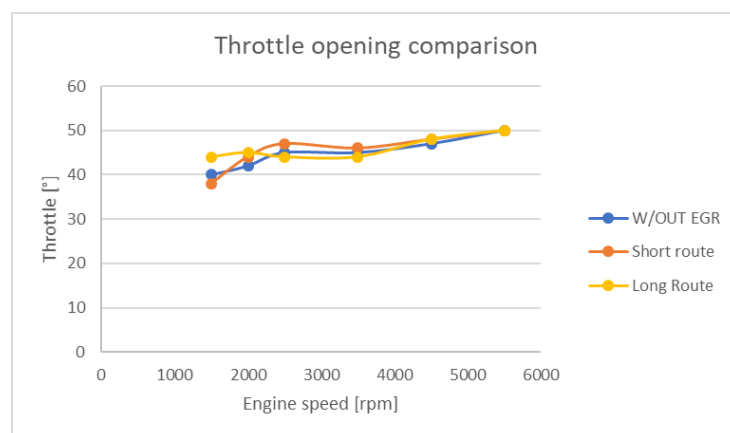


Figure 5. 20: Throttle opening for the three main cases.

According to the theory and to the short route scheme, there's the need of recovering the volume occupied by the recirculated gases.

As possible to see, this recovery can be made both increasing the boosting pressure, so rising the air density by the compressor, or recovering some degrees of throttling, which will decrease the intake pressure losses. As happens in the long route case at low regime.

The long route scheme is more reliable and precise, so its capacity of being regulated following the target working points is high (figure 5.21):

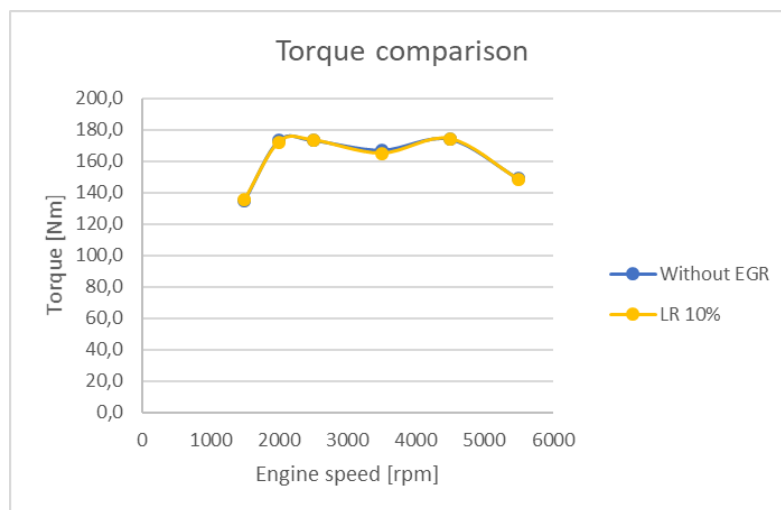


Figure 5. 21: Torque comparison between standard and long route working points.

The differences between the two EGR systems and the standard case are visible even in figure 5.22, where there's a plot of the compressor working points into his characteristic plain:

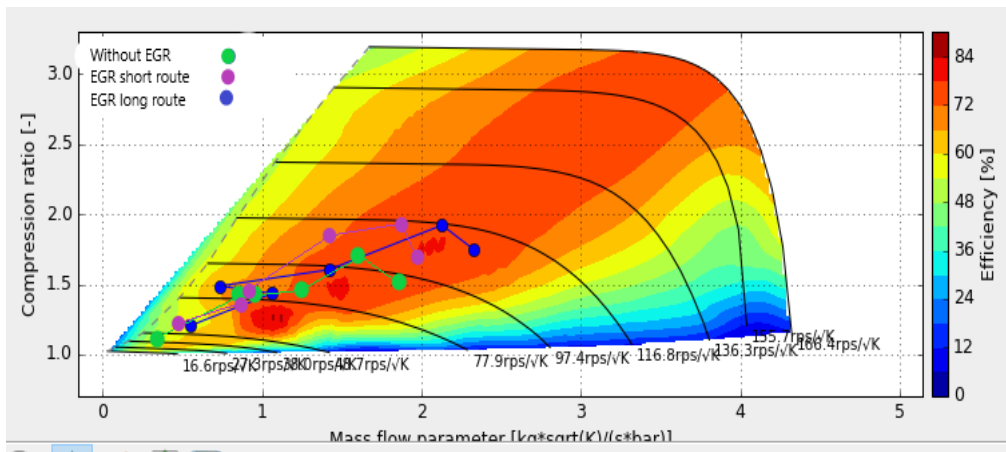


Figure 5. 22: Compressor working points in the $\dot{m}_{inlet}/\text{compressor ratio}$ plain.

Here, it is possible to notice better the difference in the turbocharger functioning between the different schemes:

- In green, the working points of the standard configuration, which as known are set at a lower compressor ratio but it is interesting to observe that they are even the ones at lower massflow parameter;
- In violet, the points representing the short route scheme, whose compressor ratio are higher and comparable with the blue ones, whereas the massflow parameters are set in the middle, because the compressor elaborates the same amount of air but at different conditions;
- In blue, the points representing the long route scheme, that have high value of compressor ratio but even the highest massflow parameters, due to the fact that the compressor has to manage with a higher flow composed by the same amount of air of the previous cases and the recirculated gases.

The implementation on the EGR, too, doesn't force the compressor to work into dangerous points, remaining still distant from the choke and the surge line, into a region of good machine efficiency generally above 60%.

Then, it is possible to see that the lower temperature of the recirculated gases in a long route, compared with a short route solution, brings to a lower inlet temperature (measured just before the splitter of the inlet manifolds), as visible at different regimes in figures 5.23 and 5.24, taking a mid-low and a mid-high regime as example:

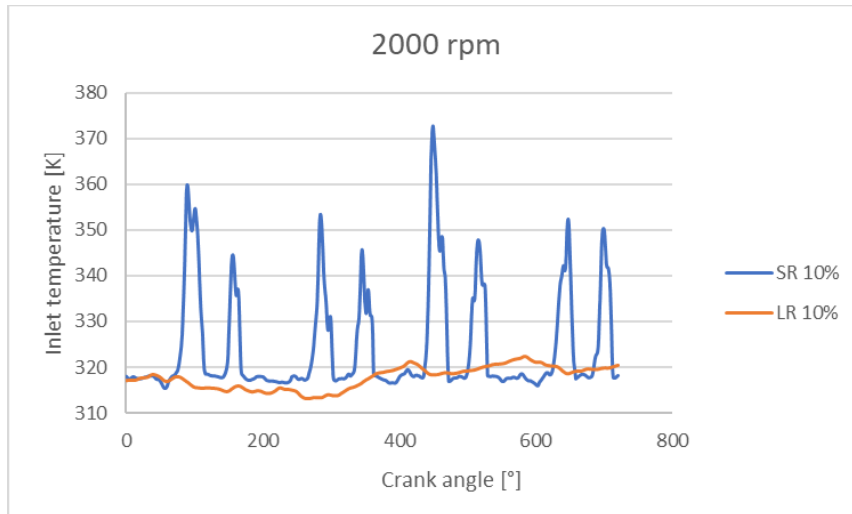


Figure 5. 23: Inlet gases temperature at 2000 rpm.

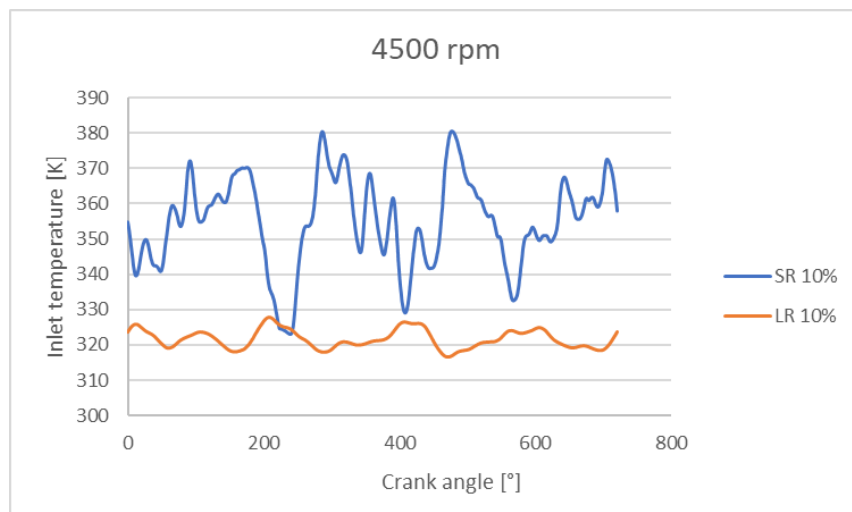


Figure 5. 24: Inlet gases temperature at 4500 rpm.

Since the recirculation happens before the compressor and so is less affected by the unsteady pressure waves generated by the engine, the temperature fluctuations are lower and so the value is more regular, especially at lower regimes.

The reduction on the inlet temperature has the advantage of enhancing the inert effects, reducing a little more the NOx emissions, as visible into the graph in figure 5.25:

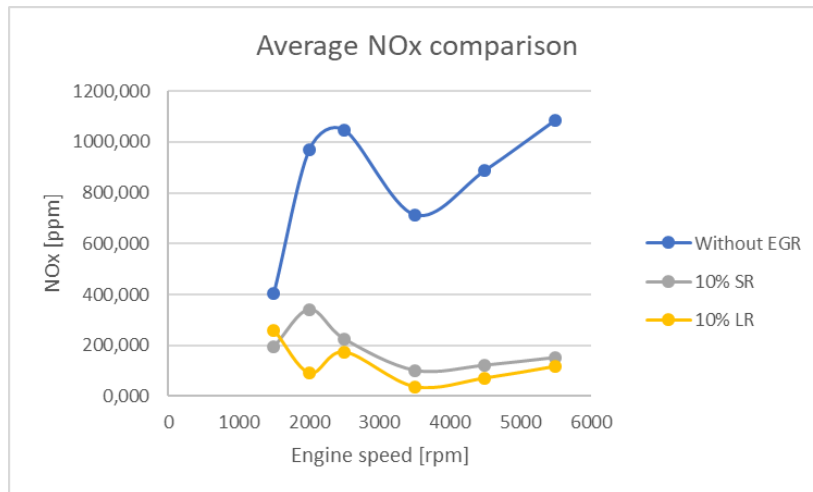


Figure 5. 25: NOx emission comparison between long route and short route.

Whereas some reductions, especially at higher regimes, could seem too high, it is interesting to note that the tendency of a reduction is present: the results a little far from a feasible value are mainly due to the not perfect stoichiometry, hard to achieve with an open-loop combustion control, and to computational limits of the program. Anyway, the important thing is that the possibility of a reduction is real, because the in-cylinder temperature reduction is possible and actually happens, as shown in the following figures (figure 5.26, 5.27, 5.28), so from the cinetical point of view the NOx reduction can be really realized, despite not so highly as suggested from the GasDyn combustion model.

There are showed three different regime (medium-low, medium, medium-high), and it is possible to see that:

- In the whole three cases the heat release is better, the combustion is anticipated due to the better mixing of the long route;
- The temperature reduction decreases with respect to the engine speed, so the maximum temperature reduction seems to be at the low regimes.
- Even at high regimes, the long route is more effective.

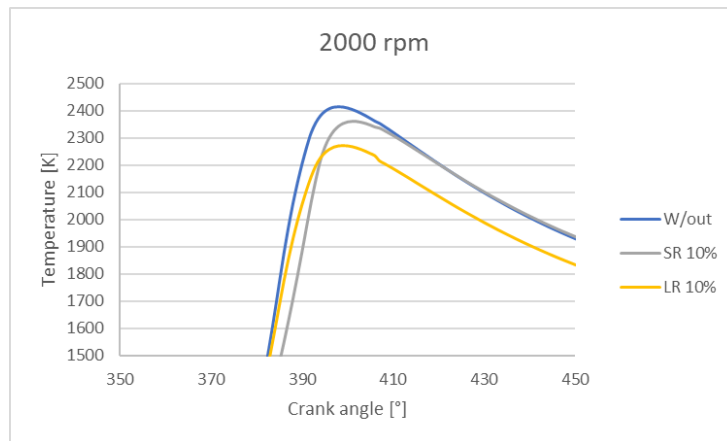


Figure 5. 26: In-cylinder temperature at 2000 rpm.

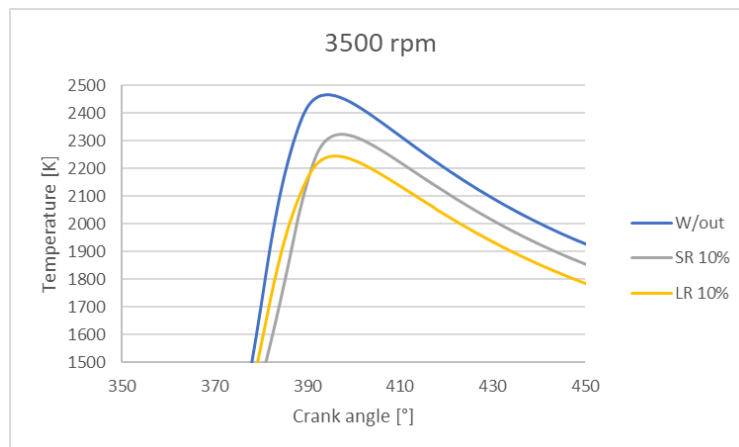


Figure 5. 27: In-cylinder temperature at 3500 rpm.

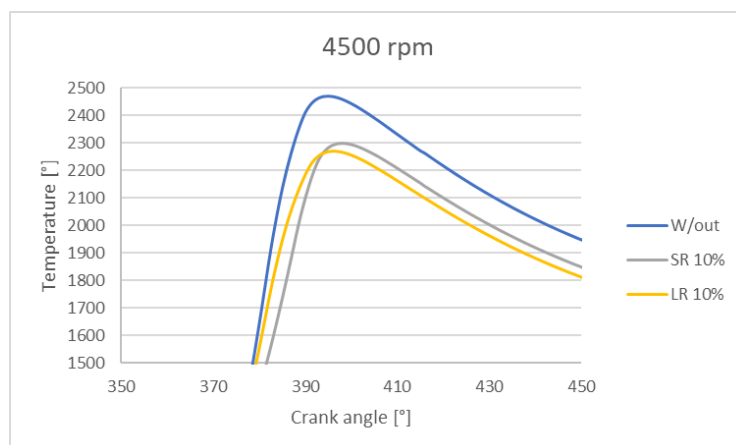


Figure 5. 28: In-cylinder temperature at 4500 rpm.

Finally, looking at the results of this work, is possible to say:

- The exhaust gas recirculation on a gasoline engine can effectively reduce the NO_x emissions, without changing the engine's properties such like stoichiometric and premixed combustion;
- The long route is more effective, and allows easily to reach higher recirculation ratios and manage them;
- The presence of the recirculated gases into the intake circuit must be compensated with an increase of the boosting pressure, but this increase is still affordable from the compressor and the turbine, due to the fact that is made at partial load;
- The long route scheme is the one that affects more the compressor because of the increase of the mass flow;
- The long route allows to reduce the intake average temperature, with respect to the short route;
- The combustion temperature reduction increases with respect to the EGR ratio, as expected;

So, the system can actually work, especially using a long route system, and the NO_x reduction, coupled with the effect of a three-way catalyst which is already mandatory, could allow to respect the future pollution norms maybe without the implementation of other complex and expensive systems, like the SCR that are now under study for the diesel engines.

Bibliography

- [1]. D.E. Winterbone, R.J. Pearson, *Theory of engine manifold design*, Professional Engineering Publishing, 1999;
- [2]. L. Cornolti, A. Onorati, T. Cerri, G. Montenegro, F. Piscaglia, *1D simulation of a turbocharged Diesel Engine with comparison of short and long EGR route solutions*, APEN article, 2013;
- [3]. L. Cornolti, G. Pellegris, *Simulazione di un motore turbodiesel veicolistico con intercooler e circuito EGR*, Politecnico di Milano master thesis, 2011;
- [4]. *GasDyn Theory manual*, Exotermia SA, 2018.